Chem Soc Rev

REVIEW ARTICLE

View Article Online
View Journal | View Issue

Cite this: *Chem. Soc. Rev.*, 2026, **55**, 4031

Surface-initiated living crystallization-driven self-assembly: from precision nanofabrication to functional interfaces

Jiawei Tao, *† Yao Lu,† Chenchen Gao,† Peiwen Wang, Zhenyan Ji, Sen Lv, Xiaomin Cai, Jingwen Zhang and Huibin Qiu *

The precise fabrication of nanostructured materials on surfaces is paramount for advancing next-generation technologies in catalysis, electronics, biomedicine, *etc.* Recently, surface-initiated living crystallization-driven self-assembly (SIL-CDSA) has enabled unprecedented control over the architecture, orientation, and functionality of solid-state nanostructures on desired substrates. This review outlines key principles of SIL-CDSA, including seed immobilization, confined epitaxial growth and micellar brush formation, together with practical methods for dimension control and spatial ordering. Intrinsic core/corona chemistry and the incorporation of exogenous species allowing targeted functionalization are also discussed, covering catalytic, electronic and bioactive features. Case studies are introduced to demonstrate SIL-CDSA as a versatile platform for hierarchically ordered nanostructures, delivering exceptional control over size, periodicity, and composition. By directly translating precision self-assembly to surfaces, SIL-CDSA opens powerful routes to multifunctional, high-performance materials for catalysis, energy systems, sensing, and device fabrication, positioning it as a transformative tool for advanced nanomanufacturing.

Received 9th January 2026

DOI: 10.1039/d6cs00030d

rsc.li/chem-soc-rev

1. Introduction

The quest for bottom-up fabrication of materials with molecular-level precision has been a central ambition in nanoscience, drawing inspiration from the exquisite control observed in biological systems.[1–3] Such precision is essential for unlocking the full potential of functional materials in fields ranging from

State Key Laboratory of Synergistic Chem-Bio Synthesis, School of Chemistry and Chemical Engineering, Frontiers Science Center for Transformative Molecules, State Key Laboratory of Micro-Nano Engineering Science, Shanghai Jiao Tong University, Shanghai 200240, China. E-mail: jiawei.tao@sjtu.edu.cn, hbqiu@sjtu.edu.cn
† These authors contributed equally.

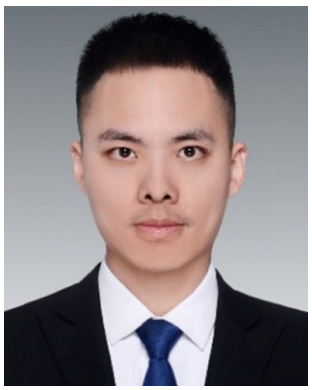

Jiawei Tao

Jiawei Tao received his PhD in Inorganic Chemistry from Jilin University in 2020. He then worked in Prof. Huibin Qiu's group at Shanghai Jiao Tong University from 2021 to 2024 as a postdoctoral researcher. He is now working as an assistant research fellow of the School of Chemistry and Chemical Engineering in Shanghai Jiao Tong University. His current research interest focuses on the self-assembly of nanomaterials and applications of nanotechnology.

Yao Lu

Yao Lu is a PhD candidate in Prof. Huibin Qiu's Group, specializing in the interfacial growth of micellar brushes via living crystallization-driven self-assembly and their inorganic functionalization for advanced applications. Prior to this, Yao Lu earned a Master's degree from Nanjing Tech University, where she acquired foundational knowledge in polymer polymerization and applied to the preparation of dual-network hydrogels.

quantum electronics to targeted therapeutics.[4–7] Conventional self-assembly processes, while powerful, often yield structures with broad size distributions and limited morphological complexity due to stochastic nucleation and growth events.[8–10] This limitation spurred the development of "living" self-assembly methodologies, analogous to living polymerization, where the growth of nanostructures proceeds from a fixed number of active seed sites in the absence of termination and chain transfer.[11,12] This paradigm shift enables the fabrication of nanostructures with precisely controlled dimensions, low dispersity, and complex, segmented architectures.[4,13,14]

Among these living methods, crystallization-driven self-assembly (CDSA) has proven particularly versatile and powerful.[15–19] CDSA leverages the crystallization of a core-forming block within a block copolymer (BCP) to drive the assembly process.[20,21] The epitaxial crystallization of subsequently added unimers (soluble BCPs) at the termini of existing seed nanocrystals further leads to the growth of low-curvature nanostructures,[22,23] such as one-dimensional (1D) cylindrical micelles,[15,24–30] two-dimensional (2D) platelets[31–38] and hierarchical micelles with anisotropic shapes.[39–45] The "living" nature of this process allows the precise tuning of nanostructure length or area by simply adjusting the unimer-to-seed ratio.[26,46] This approach was pioneered in the studies of poly(ferrocenylsilane) (PFS)-based block copolymers, where epitaxial growth enabled the fabrication of monodisperse nanofibers with tunable lengths.[47] However, a key challenge appears during the translation of this solution-phase precision to solid substrates.[48] While solution-based CDSA yields remarkable materials, their random deposition onto surfaces forfeits control over orientation and spatial organization, hindering their integration into functional devices.

Such limitation has recently been directly addressed by the advent of surface-initiated living CDSA (SIL-CDSA), a strategy that tethers the assembly process to a substrate.[49] By immobilizing seed nanocrystals onto a surface, the subsequent epitaxial growth is spatially confined, enabling the fabrication of densely packed, vertically aligned nanostructure arrays, often termed "micellar brushes".[49–58] This approach bridges the molecular precision of living self-assembly with the macroscopic order required for device integration (Fig. 1). Core scientific objectives in this burgeoning field revolve around:

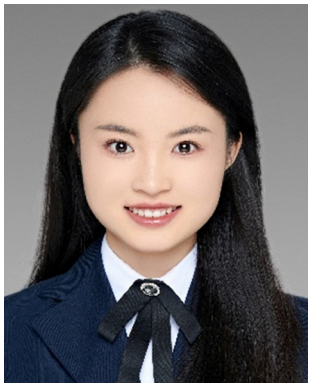

Chenchen Gao

Chenchen Gao is a PhD candidate in Prof. Huibin Qiu's group. Her primary research focuses on the growth of dynamic micellar brushes. Prior to this, Chenchen Gao earned her Master's degree from Ningxia University, where she studied the fundamentals of polymer polymerization and self-assembly.

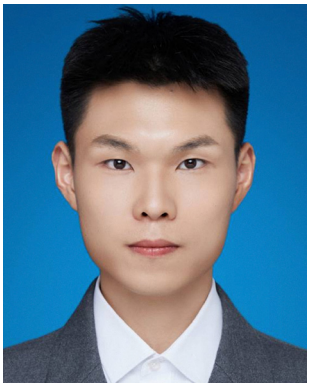

Peiwen Wang

Peiwen Wang is a doctoral candidate at the Suzhou Institute for Advanced Research, University of Science and Technology of China. In 2024, he joined the research group of Prof. Huibin Qiu at Shanghai Jiao Tong University for joint training. He is currently interested in the living crystallization-driven self-assembly of responsive block polymers.

Zhenyan Ji

Zhenyan Ji obtained her BSc in Polymer Science from Changzhou University and received her PhD in Inorganic Chemistry from the Shanghai Institute of Applied Physics, Chinese Academy of Sciences. She is currently working as a postdoctoral researcher in Prof. Huibin Qiu's group. Her current research interests center on surface-initiated living crystallization-driven self-assembly of PLLA-based block copolymers and their applications in bio-anti-inflammatory therapies and water electrolysis.

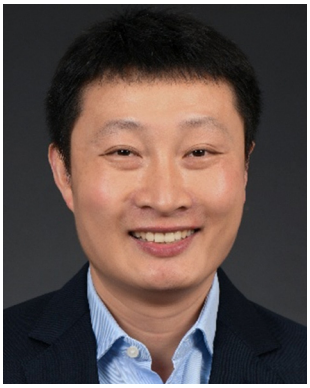

Huibin Qiu

Huibin Qiu received his PhD in Applied Chemistry from Shanghai Jiao Tong University in 2010. He then worked in Prof. Ian Manners' lab at University of Bristol from 2011 to 2015 as a Marie Curie Research Fellow. He established his independent research group at ShanghaiTech University in 2015 and then moved to Shanghai Jiao Tong University in 2018. He is now a full professor at the School of Chemistry and Chemical Engineering. His current research interests focus on the fabrication of functional materials via hierarchical self-assembly of small molecules, block copolymers and colloids.

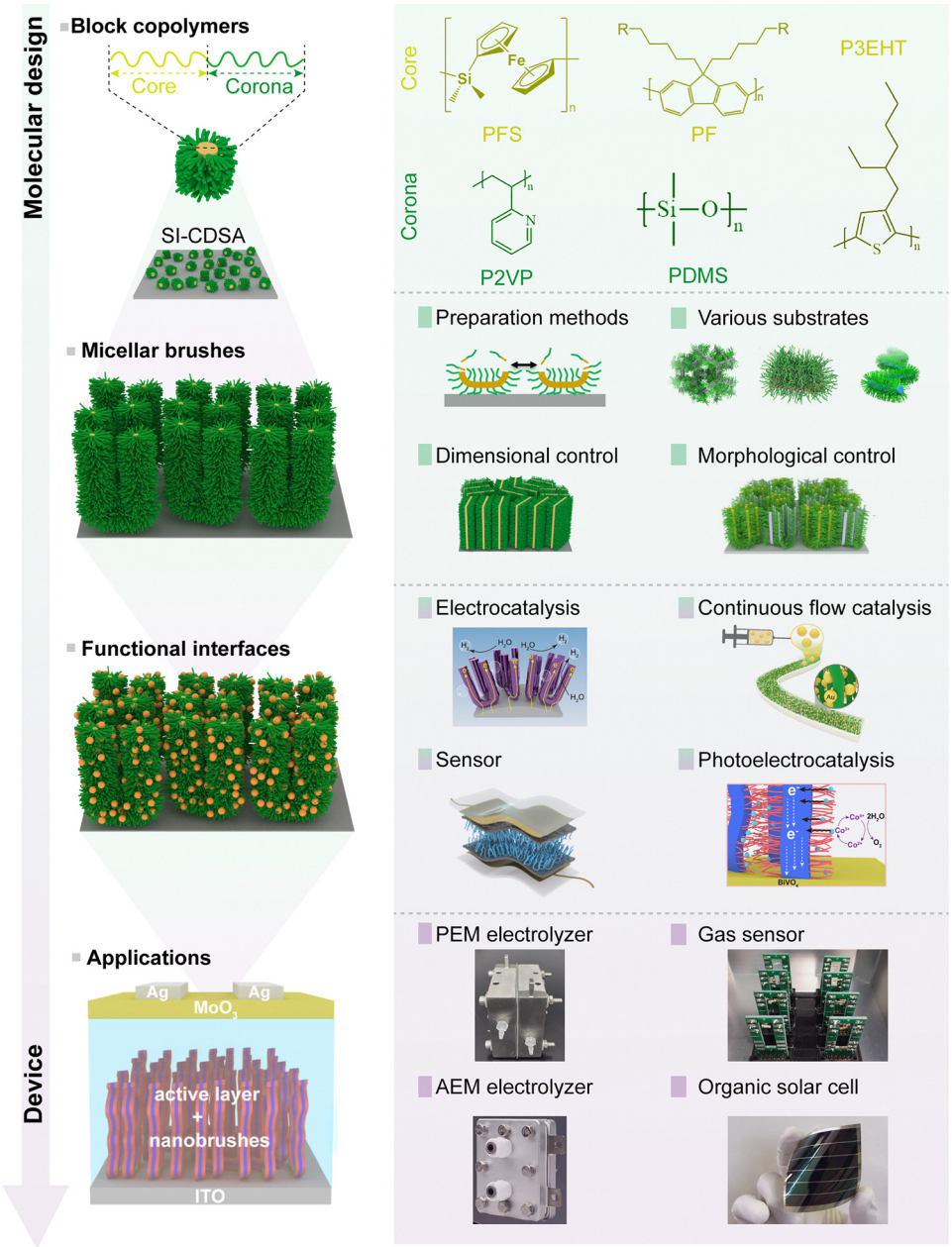

Fig. 1 Schematic overview of SIL-CDSA, including molecular design, preparation and modulation of micellar brushes, construction of functional interfaces, and their integration into devices. PF: poly(di-nhexylfluorene); P3EHT: poly(3-ethylhexylthiophene); P2VP: poly(2-vinylpyridine); PDMS: polydimethylsiloxane; PEM: proton exchange membrane; AEM: anion exchange membrane.

(1) achieving robust and versatile control over seed immobilization on diverse substrates; (2) elucidating fundamental mechanisms governing growth kinetics and morphology at solid–liquid interfaces; (3) tailoring the dimensions, shape, and hierarchical complexity of surface-grafted nanostructures; (4) developing strategies for functionalization toward specific applications; (5) probing the performance limits and technological potential of SIL-CDSA-based devices. This review positions SIL-CDSA as a cornerstone of nanotechnology, offering viable insights for researchers pursuing multifunctional, scalable nanomaterials.

2. Overview of living CDSA

Traditional approaches relying on solvent compatibility [*e.g.*, polystyrene-*b*-poly(ethylene oxide) (PS-*b*-PEO) in water/tetrahydrofuran (THF)], typically form spherical micelles or vesicles through entropy-driven separation.[59–67] In contrast, living CDSA fundamentally differs by employing anisotropic crystallization of core-forming blocks to precisely yield low-curvature architectures. The watershed study in 2007 by Manners and co-workers demonstrated this by the self-assembly of PFS-*b*-polyisoprene (PFS-*b*-PI) in hexane, where epitaxial growth of PFS cores produced monodisperse nanocylinders with lengths

tunable from 200 nm to 2 μm.[46] Subsequent work extended living CDSA to diverse crystallizable polymers: *e.g.*, poly(ε-caprolactone) (PCL) formed 2D platelets in THF/water,[68] poly(3-hexylthiophene) (P3HT) generated semiconducting fibers.[69] Unlike solvophobic systems limited by equilibrium thermodynamics, living CDSA operates under kinetic control governed by chain folding energetics and crystal lattice matching, and revolutionizes the fabrication of nanostructures by mimicking the temporal control of chain growth polymerization. Introducing pre-formed micelle seeds to unimer solutions initiates epitaxial crystallization at termini, with growth rates following first-order kinetics.[34,35,50,70] Polymerization-induced CDSA further integrates synthesis and assembly. Ring-opening polymerization of ε-caprolactone directly generated crystalline cores templating uniform 2D platelets.[71] Sequential addition of different unimers enables architectural complexity: segmented PDMS/P2VP nanofibers exhibit diverse, multidimensional assemblies in different solvents.[40]

Two complementary strategies are widely used to control nucleation and growth in living CDSA. Self-seeding leverages the inherent crystallinity of the core-forming block: thermal or solvent-induced partial dissolution removes less ordered regions while preserving well-defined crystalline nuclei that govern uniform regrowth upon cooling.[72,73] This three-step protocol—fragmentation of initial micelles (often by sonication), annealing above a partial dissolution temperature to eliminate defective crystallites, and controlled cooling to allow epitaxial growth—effectively decouples nucleation and growth and yields size control beyond what is possible in equilibrium-driven solvophobic assembly.[74,75] Seeded growth, by contrast, employs stable, preformed micelle seeds added to unimer solutions at ambient conditions.[76] Pioneered for PFS-based BCPs, this approach has expanded to diverse crystalline-coil systems, including π-conjugated polymers[4,77–79] and biodegradable polyesters,[80,81] favoring unprecedentedly high monodispersity in solution assembly.

3. Surface-initiated living CDSA: principles and fabrication

Both self-seeding and seeded-growth methods were developed and optimized in free solution, but translating these concepts to interfaces is essential for practical applications such as surface patterning and device integration. The growth behavior of SIL-CDSA differs fundamentally from that in solution because the micelle seeds are tethered to an immobilized substrate.[17,48,82] In this configuration, the elongation of crystalline domains is no longer governed solely by unimer and self-nucleation in free solution, but instead results from the combined influence of restricted unimer diffusion through the surrounding medium and site-specific attachment at the surface-bound seed layer.[20,57,83] The finite mobility of unimers, dictated by their concentration, solvent quality, and diffusional path length, directly influences the rate and uniformity of crystallite extension.[36,84] At the same time, the chemistry and topology of the underlying substrate modulate the polymer–substrate interactions (*e.g.*, hydrogen bonding, π–π stacking, electrostatic attraction). Additionally, surface coverage of initiating sites determines the lateral packing density of nanostructures. Variations in these parameters collectively regulate the attainable dimensions (height, density), spatial arrangement, and orientational order of the assembled nanostructures.[8,37] By deliberately tuning unimer supply, initiation density, and interfacial chemistry, SIL-CDSA can achieve a structural precision in terms of uniformity, alignment, and pattern complexity, which is rarely accessible with conventional solution-based CDSA,[26,85,86] thereby establishing a robust platform for the versatile fabrication strategies detailed in the sections that follow.[87–89]

3.1. Fabrication strategies

The fabrication of SIL-CDSA architectures is a multi-step process, beginning with the preparation of well-defined micelle seeds, followed by their immobilization on a substrate, and culminating in controlled directional growth. The precision and reproducibility at each stage are crucial for achieving uniform nanostructure arrays.

3.1.1. Seed preparation. The foundation of any living self-assembly process is the seed, which acts as the nucleation for subsequent growth. In CDSA, seeds are typically short, low-dispersity fragments of the desired nanostructure and their quality (length dispersity, crystallinity and surface structure) strongly influences growth kinetics and finial morphology.

3.1.1.1. Fragmentation. The most widely used method relies on first forming the desired micellar aggregate and then fragmenting it into smaller, uniform pieces, often through sonication (Fig. 2a).[51,76] This route is broadly applicable because it does not require specialized equipment or polymer designs, and it is compatible with many semicrystalline core-forming blocks. Importantly, seed length and dispersity can be tuned by controlling the parent micelle morphology and the fragmentation conditions (*e.g.*, sonication power/time, temperature, and polymer concentration). Despite being relatively time-consuming, its robustness and reproducibility make it the default choice in most studies (Table 1).

3.1.1.2. Flow supersaturation seeding. Recent innovations have focused on accelerating and simplifying seed production. For instance, Xiao *et al.* demonstrated a rapid seed preparation method using a flow system where supersaturation of a polymer solution drives uniform seed micelle formation in minutes, a significant reduction from the week-long processes previously reported (Fig. 2b–d).[5] Mechanistically, rapid mixing under flow enables precise control over the nucleation window, helping suppress secondary nucleation and broad size distributions. Beyond speed, this strategy is attractive for scale-up because it improves throughput by orders of magnitude and is amenable to continuous, end-to-end production, enabling direct conversion from polymer feedstock to seeded nanostructure growth.

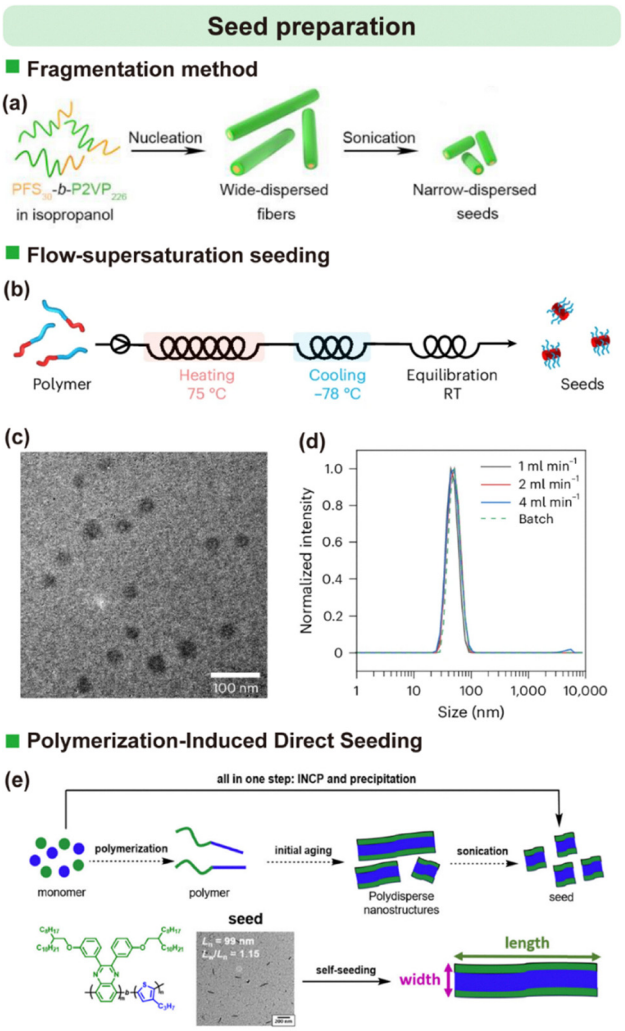

Fig. 2 (a) Schematic illustration of the conventional fragmentation method used to prepare micelle seeds. Reproduced from ref. 51 with permission from American Chemical Society, copyright 2021. (b) Scheme for preparation of micelle seeds generated in-flow using diblock copolymers. (c) Transmission electron microscope (TEM) image of the resulting seeds. (d) Dynamic light scattering size distributions of flow-prepared seeds obtained at various flow rates. Reproduced from ref. 5 with permission from Springer Nature, copyright 2025. (e) Comparison of methods for producing uniform seeds: conventional CDSA (dashed arrow) *versus* polymerization-induced direct seeding (solid arrow) in a single step. Reproduced from ref. 68 with permission from American Chemical Society, copyright 2024.

3.1.1.3. Polymerization induced direct seeding. Another strategy involves leveraging the polymer synthesis itself. Kim *et al.* showed that polymerization-induced CDSA (PI-CDSA) of fully conjugated block copolymers could produce nanoribbons, and simple purification by precipitation yielded short, uniform seed structures directly, bypassing the conventional aging and fragmentation steps entirely (Fig. 2e).[86] However, PI-CDSA seed generation is currently more system-dependent, requiring compatibility between polymerization conditions, solubility evolution, and crystallization/assembly kinetics.

Collectively, these approaches substantially shorten seed preparation time and broaden the toolkit for living CDSA. Nevertheless, the conventional "self-assembly + fragmentation" route remains most commonly adopted because of its generality across polymer chemistries and morphologies, whereas newer methods (flow-based supersaturation and PI-CDSA-derived seeds) offer compelling advantages in speed, integration, and scalability but may require more stringent control of solution thermodynamics or polymerization/assembly coupling (Table 1).

3.1.2. Seed immobilization. The immobilization of seeds onto the substrate is the defining step that distinguishes SIL-CDSA from its solution-phase counterpart. This process is strongly influenced by substrate topography, surface chemistry, and the functional groups present in the micelle corona. A wide variety of substrates—such as silicon wafers, glass, graphene nanosheets, metals, carbon cloth, nickel foam, or silica—can be functionalized with, or directly loaded with micelle seeds.[49,51,54,57,90] Different immobilization methods are chosen based on substrate morphology and processing goals:

3.1.2.1. Drop casting

A simple and versatile approach in which a micelle seed solution is dispensed directly onto the substrate surface, followed by solvent evaporation (Fig. 3a). This method is applicable to both smooth and rough surfaces, including silicon wafers, glass slides, and metal foils, and is particularly useful for rapid prototyping or small-area patterning.

3.1.2.2. Spin coating

Best suited for smooth, planar substrates. By applying centrifugal force, seeds are evenly distributed over the surface, enabling the formation of highly uniform and densely packed seed layers (Fig. 3b and c). This uniformity is critical for producing vertically aligned micellar brushes with controlled density.[49]

Table 1 Comparison of three seed preparation methods

Method	Principle	Time required	Typical applicability
Fragmentation[51,76]	Induce self-assembly to form large aggregates, then break into short, uniform seeds	Days to a week	Default choice in most CDSA studies; general seed preparation for various block copolymers.
Flow-supersaturation seeding[5]	Use a flow system to rapidly reach supersaturation, leading to uniform micelle nucleation in minutes.	Minutes	High-throughput or industrial CDSA processes; rapid prototyping.
Polymerization-induced direct seeding[86]	Generate seeds directly during PI-CDSA of block copolymers, followed by simple purification.	Hours	When polymer synthesis and seed preparation can be integrated; tailored nanostructures.

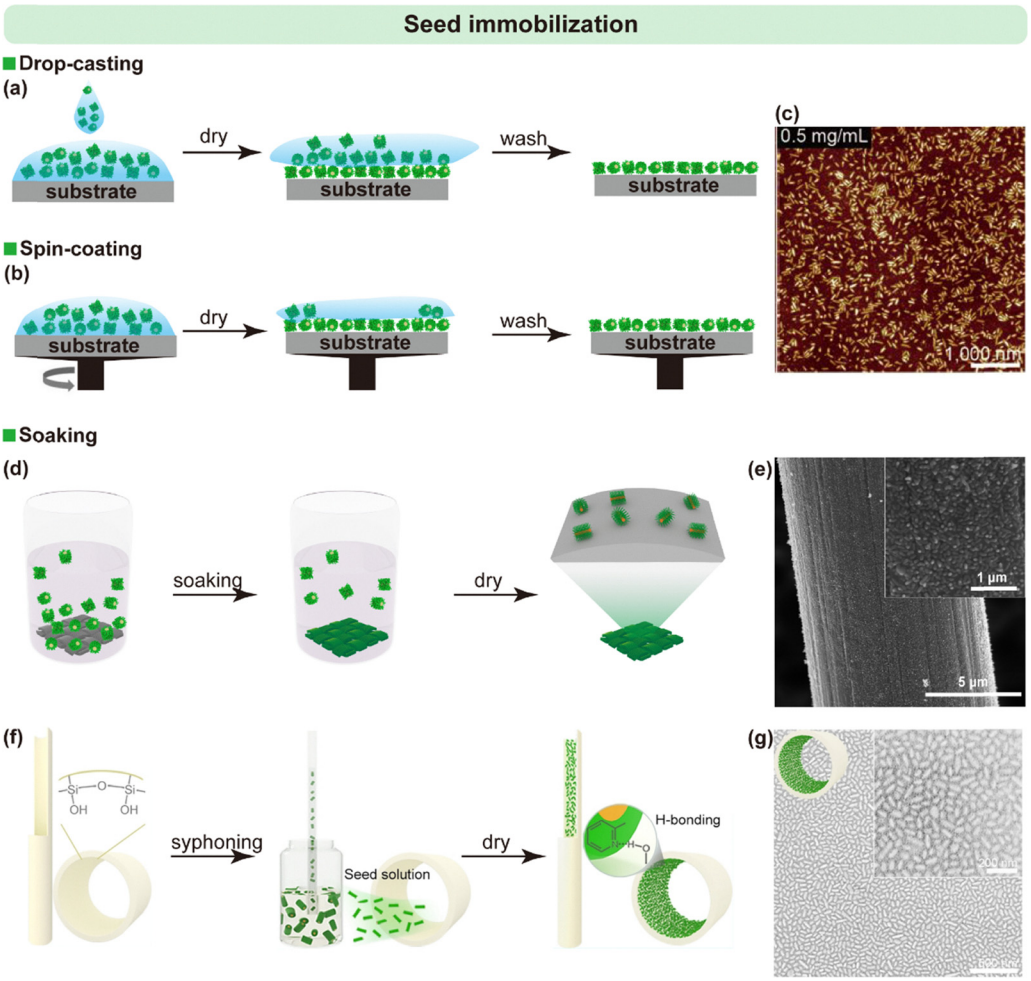

Fig. 3 (a) Schematic of drop-casting used for micelle seed immobilization. (b) and (c) Schematic of spin-coating (b) and corresponding AFM image (c). (c) is reproduced from ref. 49 with permission from AAAS, copyright 2019. (d–g) Schematics of the soaking method, with corresponding SEM images shown in (e) and (g). (e) is reproduced from ref. 54 with permission from Spring Nature, copyright 2025. (g) is reproduced from ref. 51 with permission from Wiley, copyright 2021.

3.1.2.3. Soaking

Ideal for porous or nanostructured substrates such as carbon cloth, nickel foam, or graphene nanosheets (Fig. 3d and e). In this approach, micelle seeds readily diffuse into and adsorb throughout the micro- and nano-scale pores, enabling high surface coverage even on complex, irregular geometries. The method can also be applied to tubular materials, such as glass capillaries, by simply immersing one end of the tube into the seed solution, allowing capillary action to draw the solution inward (Fig. 3f and g).

Seed–substrate adhesion in SIL-CDSA is typically achieved through either non-covalent or covalent interactions. Non-covalent approaches, including hydrogen bonding, electrostatic attraction, and coordination, offer simple and versatile immobilization routes that do not require chemical surface modification. For example, pyridine groups in a P2VP corona can hydrogen-bond with surface silanol groups on silica, or directly coordinate to gold through pyridine–Au interactions. Although these methods enable rapid and straightforward attachment across a variety of substrates, the binding strength is generally lower than that of covalent linkages. Such interactions are also sensitive to environmental conditions. For instance, under acidic conditions, protonation of the pyridine nitrogen diminishes its ability to hydrogen-bond or coordinate with metal surfaces, which may lead to seed detachment.

By contrast, covalent bonding provides the most robust form of immobilization, ensuring stability even under demanding processing conditions. This strategy typically involves pre-functionalizing the substrate with reactive moieties capable of forming covalent linkages with corona chain functional groups. For instance, micelle seeds bearing a P2VP corona can be anchored to otherwise inert interfaces *via* reaction with 3-iodopropyltrimethoxysilane (Fig. 4).[49] The enhanced durability of such attachment was demonstrated by subjecting the immobilized seeds to quaternization with methyl iodide (MeI), a treatment known to disrupt hydrogen-bond-based immobilization. No detectable detachment was observed for covalently bound seeds. Covalent strategies are particularly advantageous

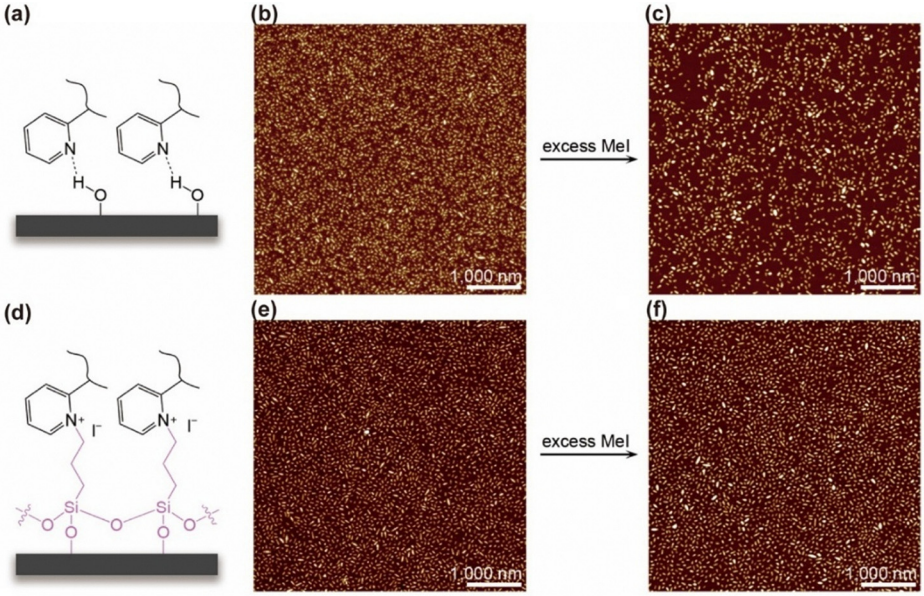

Fig. 4 (a) Schematic of H-bond-based immobilization of PFS-*b*-P2VP seeds on silicon. (b) and (c) AFM height images of PFS_{36}-*b*-$P2VP_{502}$ seeds (0.5 mg mL^{-1} in isopropanol) immobilized *via* H-bonding before (b) and after (c) MeI treatment. Significant seed detachment was observed. (d) Schematic of covalent immobilization using 3-iodopropyltrimethoxysilane. (e) and (f) AFM height images of PFS_{36}-*b*-$P2VP_{502}$ seeds immobilized covalently before (e) and after (f) MeI treatment. Covalent bonding prevented noticeable detachment. Reproduced from ref. 49 with permission from AAAS, copyright 2019.

for stabilizing seeds on chemically inert substrates such as polymers or elastomers.

3.1.3. Micellar brush growth. Once the micelle seeds are firmly immobilized, epitaxial extension from their active termini yields micellar brushes (dense arrays of cylindrical micelles oriented perpendicularly to the substrate surface). Growth proceeds through a unimer-addition mechanism: solvated unimers diffuse from the bulk solution to the seed-solution interface, infiltrate the crystalline core, and elongate the micelle while preserving the cross-sectional dimensions and crystalline lattice of the seed. The growth characteristics are governed primarily by:

3.1.4. Unimer-to-seed ratio. Determining the ultimate micelle length (Fig. 5); excessively high ratios can trigger secondary nucleation or structural defects, whereas insufficient ratios yield shorter brush architectures.[49]

3.1.5. Density of seeds. Controlling the areal density of micellar brushes, adjustable *via* the feed concentration of seeds.

By tuning both factors in concert, SIL-CDSA enables predictable and reproducible brush growth with controlled length, alignment, and uniformity across the surface. Such precision is critical for engineering surface-bound nanostructures with tailored mechanical stability, optical anisotropy, or interfacial properties that match specific application needs. Notably, micellar brush growth *via* SIL-CDSA has been validated on a wide range of chemically and structurally diverse substrates—including carbon cloth, carbon paper,[54] nickel foam,[53] metal–organic-framework (MOF) particles,[55] PDMS membranes[52] and others (Fig. 6), demonstrating the adaptability and universality of this methodology. This broad substrate compatibility greatly facilitates integration of micellar brushes into complex architectures, such as catalytic electrodes, flexible coatings, or porous scaffolds, and opens opportunities for hybrid material systems that combine organic precision with inorganic robustness.

3.2. Mechanistic insights

Manners *et al.* employed atomic force microscopy (AFM) to conduct detailed, real-time investigations of the SIL-CDSA of individual micelle seed immobilized on silicon substrates.[58] Their findings revealed that fiber-like micelle growth from single, surface-bound seed proceeds through four distinct kinetic regimes, evolving from an initial surface-confined mode to a surface-limited regime. This progression was reflected in changes in the growth rate with increasing length of the epitaxially grown segments extending from each seed terminus (Fig. 7a).

To illustrate, *ex situ* data were obtained from micelles grown by interfacial seeded growth of a PFS-*b*-P2VP unimer solution in THF from PFS-*b*-P2VP surface-bound seeds. The growth curves were fitted to mathematical models capturing the four kinetic stages:

– Initial regime – very rapid elongation (Fig. 7a(i)).

– First decay – exponential decrease in rate up to a turning point (Fig. 7a(ii)), attributed to depletion of unimer near the surface.

– Surface-dissociation acceleration – exponential rate increase (Fig. 7a(iii)) as the micelle termini lift away from the substrate, enhancing unimer access.

– Final steady state – Boltzmann-type rate decay (Fig. 7a(iv)) as bulk unimer depletion limits further growth.

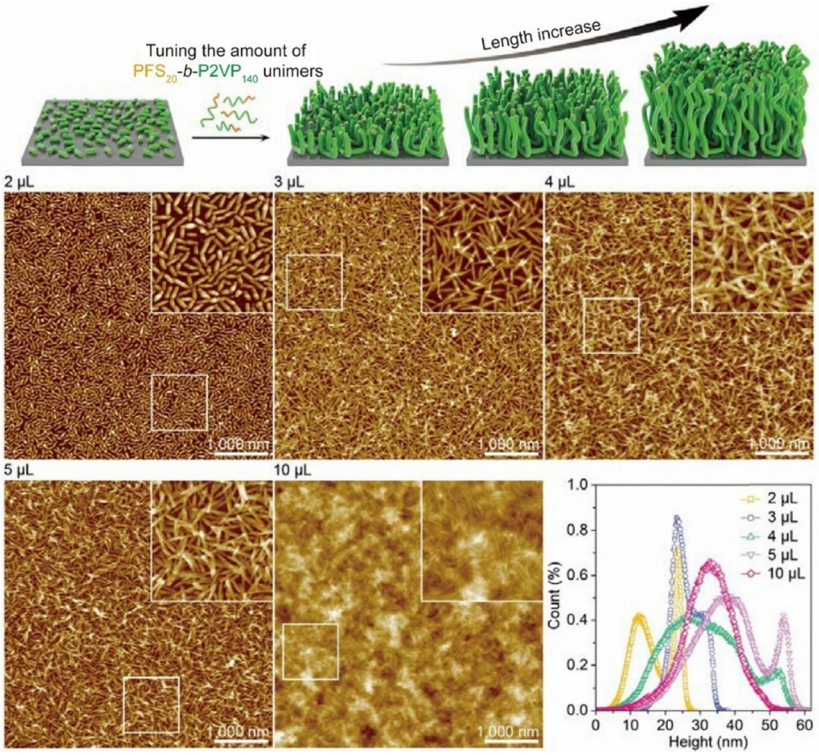

Fig. 5 Top: schematic illustrating brush elongation and height increase with added unimers. Bottom: AFM height images and distributions of PFS_{20}-*b*-$P2VP_{140}$ brushes grown from seeds (L_n = 58 nm). Adding 2–5 μL unimer transformed lying micelles (~20 nm height) into stacked (~25 nm) and coral-like structures (10–60 nm height, average 35–40 nm). At 10 μL, brushes collapsed into a uniform layer (~35 nm), with heights possibly underestimated due to probe inaccessibility. Reproduced from ref. 49 with permission from AAAS, copyright 2019.

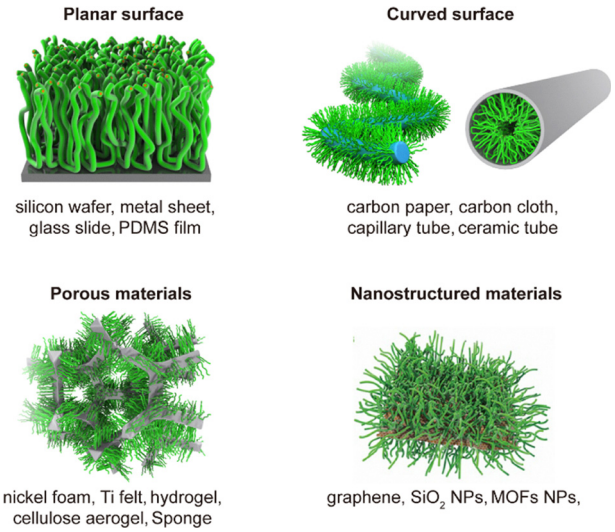

Fig. 6 Micellar brushes grown on different kinds of substrates, including planar surface, curved surface, porous materials and nanostructured materials.

When a high density of seeds is immobilized to form micellar brushes, the growth geometry changes markedly (Fig. 7b). Steric crowding between adjacent seeds and their expanding coronas limits lateral growth, forcing nascent micelles to extend predominantly away from the surface. This vertical or tilted orientation bypasses the prolonged surface-parallel regime seen for isolated seeds, leading to earlier onset of surface dissociation and a more uniform, upright brush-like architecture. In such densely packed systems, unimer delivery to growth fronts is further constrained by diffusion through the interstitial corona matrix, potentially generating heterogeneous growth rates among fibers.

4. Advanced structural control and modulation

4.1. Dimension control of micellar brush arrays

The axial dimensions of cylindrical micellar brushes generated by SIL-CDSA are governed primarily by the kinetic parameters of living crystallization, as outlined previously. In essence, systematic variation of the seed-to-unimer ratio enables precise regulation of brush height. This principle forms the basis for predictable one-dimensional growth, yet SIL-CDSA can also be adapted to create complex 2D micellar architectures by deliberately perturbing the lateral symmetry of the growth environment.

A representative strategy for achieving such lateral growth anisotropy relies on the tilted immobilization of cylindrical micelle seeds, exemplified by PFS_{24}-*b*-$P2VP_{371}$, on silicon substrates (Fig. 8a).[83] Hydrogen bonding between the pyridine moieties of the P2VP corona and surface silanol groups induces

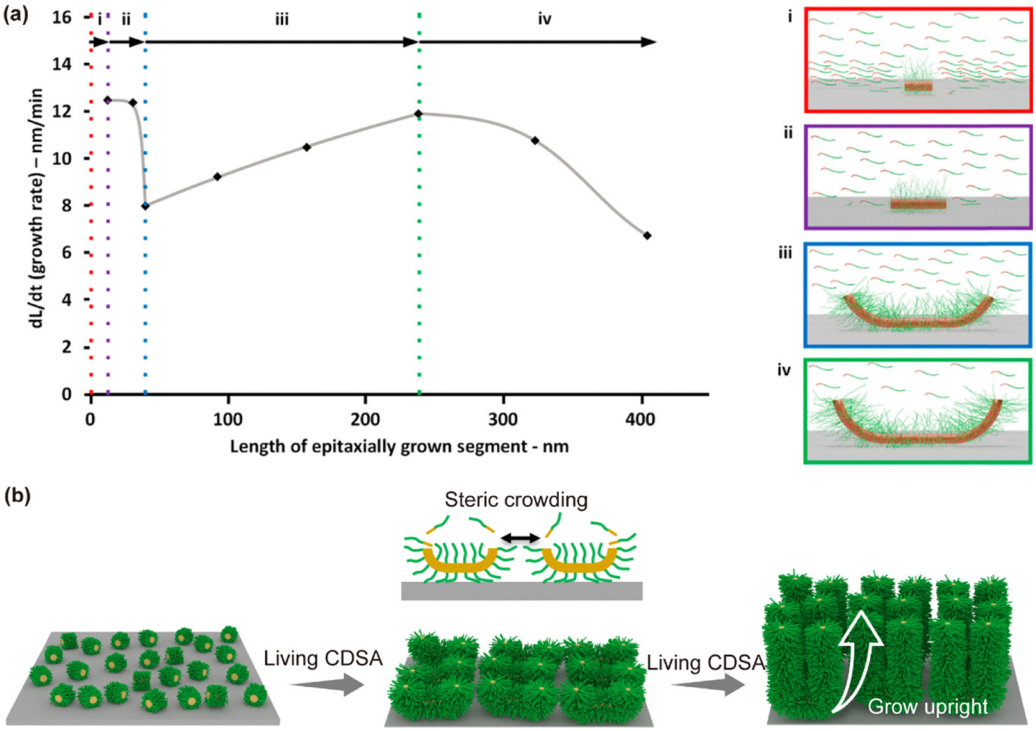

Fig. 7 (a) Mathematical fit of the interfacial growth rate of PFS-*b*-P2VP micelles *versus* segment length formed by epitaxial growth, obtained by adding PFS-*b*-P2VP in THF (2.5 μL, 10 mg mL^{-1}) to PFS-*b*-P2VP surface-bound seeds (SBSs) (5 μL, 0.01 mg mL^{-1}, L_n = 31 nm) immobilized on Si wafers in 0.5 mL iPrOH. Dotted lines and arrows indicate four distinct regimes (i–iv). Schematic representations of these regimes: (i) SBSs show a high initial growth rate due to unimer near the surface. (ii) Growth rate declines exponentially as local unimer is rapidly consumed; growth remains diffusion-limited under strong surface influence. (iii) A slower exponential rate increase occurs as longer micelle segments extend further into solution, improving unimer access. (iv) Local unimer depletion leads to a decline similar to seeded growth in bulk solution. The peak and drop-off are fitted with a Boltzmann curve, reflecting steady-state, diffusion-limited growth. Reproduced from ref. 58 with permission from American Chemical Society, copyright 2022. (b) Schematic illustrating steric crowding between adjacent seeds, causing them to extend predominantly away from the surface.

asymmetric conformations, in which one side of the seed is sterically shielded by collapsed P2VP chains, while the opposite side remains exposed and available for epitaxial extension. Subsequent introduction of a blended unimer feed comprising PFS-*b*-P2VP block copolymers together with PFS homopolymer, drives site-selective crystallization exclusively on the unshielded flank, producing unilateral platelet growth from the immobilized seeds. The extent of unilateral platelet formation is tunable: increasing the initial seed length from 129 to 535 nm enhances the yield from approximately 44% to 92% (Fig. 8b and c). Elevated growth temperatures (*e.g.*, 30 °C) typically favor unilateral propagation with efficiencies of 70–90% (Fig. 8d and e). Manipulation of the corona chain length provides another control lever—shorter P2VP coronas (degree of polymerization 139) significantly reduce the yield relative to longer coronas (degree of polymerization 371), with values falling from *ca.* 90% to 47%.

Ordered 2D micellar brush arrays can be fabricated through distinct approaches tailored to the desired surface architecture (Fig. 9). In one route, discrete slope-like platelet arrays are obtained by introducing spherical micelles (*e.g.*, PS-*b*-P2VP) as inert spacers incapable of initiating CDSA. Co-immobilisation of such spheres with cylindrical seeds *via* static vertical deposition followed by exposure to blended unimers results in unilateral off-surface platelet growth from the cylinders, with the spheres dictating an ≈30° inclination in the platelet orientation. Alternatively, dense blade-like arrays can be realized by directionally depositing pure PFS cylindrical seeds in a compact side-by-side configuration, yielding ordered domains with a periodicity of ∼40 nm. Blended unimer addition in this case drives vertical unilateral platelet formation to heights of ≈90 nm, generating uniform, large-area arrays with a high degree of order. Beyond these single-corona structures, sequential addition of distinct blended unimers facilitates segmented unilateral platelets comprising, for example, P2VP and PDMS corona regions. Such segmented architectures expand post-assembly possibilities, including the site-selective incorporation of platinum nanoparticles into the P2VP segments, and can be rendered as freestanding arrays by attenuating surface adhesion through treatment with triethylamine.

4.2. Compositional diversification

The functional versatility of micellar brushes can be substantially expanded by modifying the chemical composition of the constituent block copolymers. By varying the crystalline core-forming segment, the corona-forming segment, or both, it becomes possible to engineer interfacial interactions, responsiveness to external stimuli, and tailored optoelectronic characteristics.

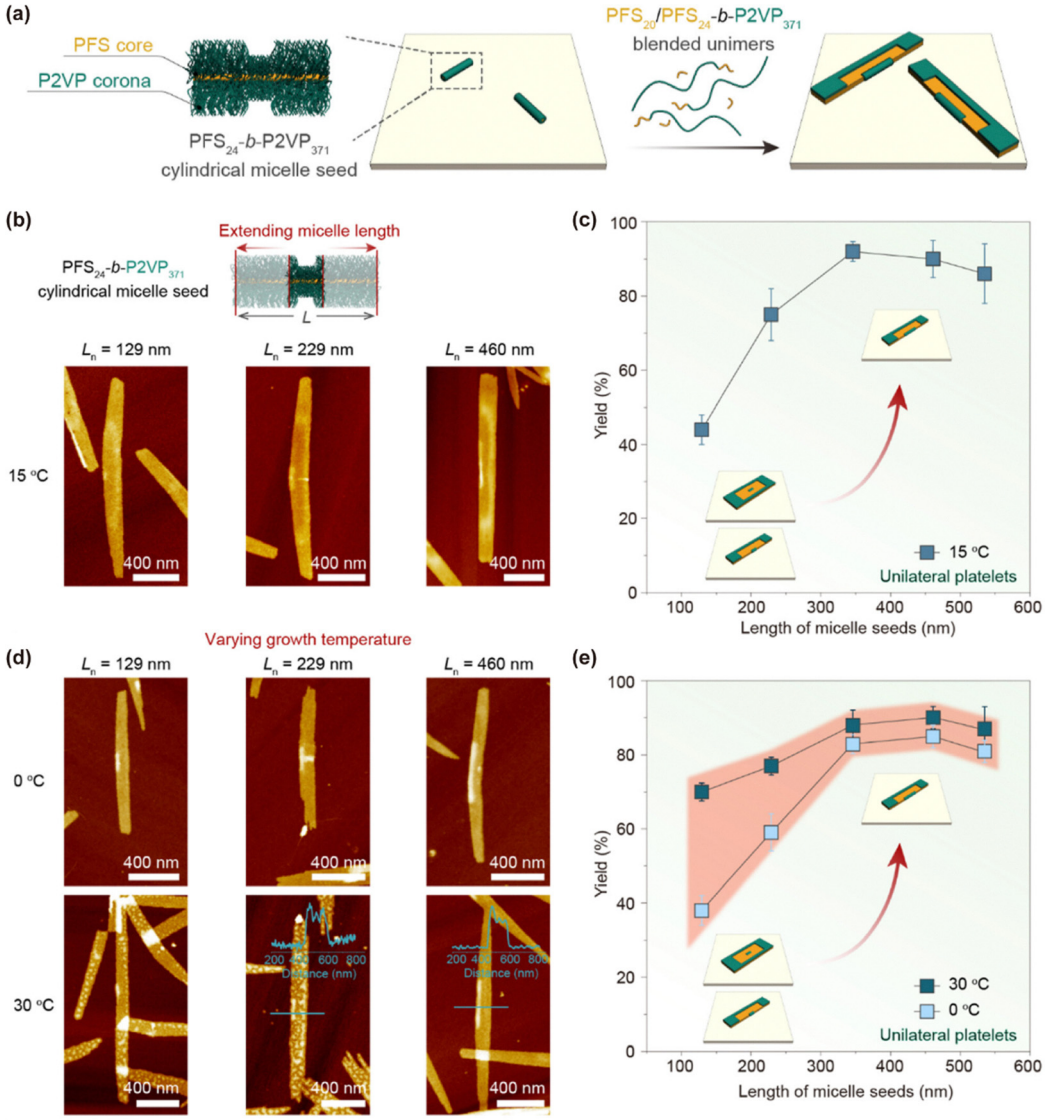

Fig. 8 (a) Schematic of surface-initiated unilateral 2D living CDSA, with PFS_{24}-*b*-$P2VP_{371}$ cylindrical micelle seeds sparsely immobilized on silicon prior to addition of blended unimers. (b) AFM images of unilateral platelets grown from seeds of L_n = 129, 229, and 460 nm. (c) Unilateral platelet yield as a function of seed length. (d) AFM images of platelets obtained at 0 °C and 30 °C from immobilized seeds of the same lengths. (e) Yield dependence on growth temperature. Reproduced from ref. 83 with permission from American Chemical Society, copyright 2024.

4.2.1. Incorporation of different block/conjugated systems. Cai *et al.* designed micellar brushes with a PFS crystalline core and a P2VP corona.[49] The PFS core provided structural integrity through CDSA, while the P2VP corona imparted pH-responsiveness and tunable hydrophilicity *via* protonation–deprotonation equilibria. Zhang *et al.* developed micellar brush arrays in which the semiconducting conjugated polymer P3EHT was incorporated directly as the core-forming block in P3EHT–*b*–P2VP brushes.[57] This design endowed the surfaces with inherent photoactive properties arising from the conjugated P3EHT chain packing. Yang *et al.* reported further functional micellar brushes based on fully conjugated block copolymers such as poly(9,9-dioctylfluorene)-*b*-poly(quinquethiophene) (PF-*b*-QPT), yielding architectures with tunable optical absorption and emission, along with potential utility in organic electronic applications.[56] These studies illustrate how judicious selection of block combinations enables the integration of responsive, catalytic, or bio-interactive capabilities into micellar brush systems.

4.2.2. Segmented growth *via* living CDSA. The living nature of CDSA enables precise, sequential extension of pre-formed micellar brushes to create compositionally segmented architectures. In this approach, a brush grown from an initial seed population retains an active crystalline growth front at its free termini. Subsequent introduction of a second block-copolymer unimer, containing the same crystallizable core block but a different corona-forming block, drives epitaxial extension without disturbing the dimensions or order established in the first segment. This unimer selectively crystallizes onto the existing core lattice, producing a contiguous micelle whose

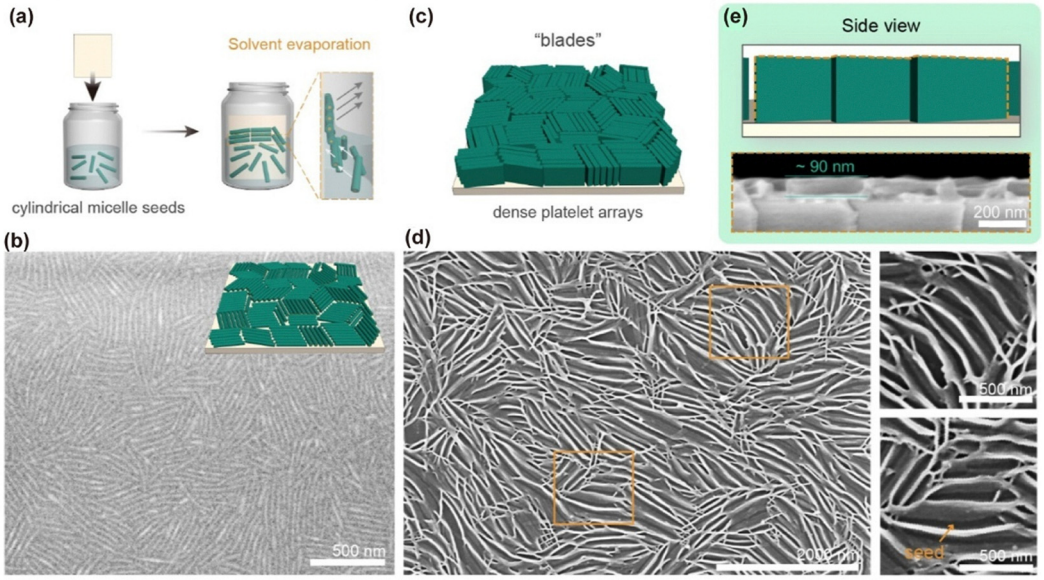

Fig. 9 (a) Illustration for the static vertical deposition of cylindrical micelle seeds *via* solvent evaporation. (b) Schematic illustration and SEM image of the silicon surface that densely immobilized with PFS_{24}-*b*-$P2VP_{371}$ cylindrical micelle seeds (L_n = 460 nm). (c–e) Schematic illustration (c), top-view (d), and side-view (e) SEM images of the dense blade-like platelet arrays formed after the addition of blended unimers of PFS_{24}-*b*-$P2VP_{371}$ and PFS_{20}. Reproduced from ref. 83 with permission from American Chemical Society, copyright 2024.

axial segments differ in corona chemistry. For example, a micellar brush composed of PFS-*b*-P2VP can be elongated at its free ends with PFS-*b*-PDMS segments (Fig. 10).[49] This process maintains the PFS crystalline backbone while replacing the terminal corona from hydrophilic P2VP to hydrophobic PDMS, thereby tuning interfacial properties *in situ*. Such controllable "block-on-block" brush extensions enable dynamic modulation of surface wettability, potential responsive coating designs, and the creation of multi-functional surfaces from a single seed layer.

4.2.3. Patterned multi-component brush arrays. Beyond axial segmentation within individual brushes, spatially resolved patterning can be achieved by combining selective immobilization of distinct seed types with parallel growth (Fig. 11).[57] In this strategy, nanoscale seeds composed of different crystallizable core

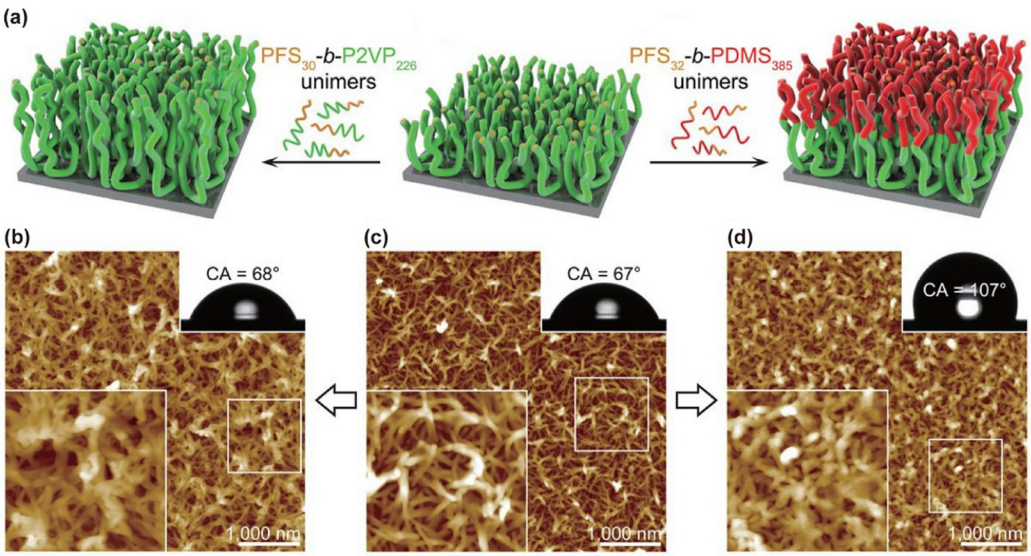

Fig. 10 (a) Diagram illustrating the sequential growth mechanism of PFS_{30}-*b*-$P2VP_{226}$ micellar brushes and the formation of segmented micellar brushes. (b–d) AFM height images displaying: (b) short micellar brushes obtained by introducing 3 μL of PFS_{30}-*b*-$P2VP_{226}$ unimer solution; (c) elongated micellar brushes generated by an additional 3 μL of PFS_{30}-*b*-$P2VP_{226}$ unimer solution to the structures in (b); and (d) segmented micellar brushes produced by subsequently adding 3 μL of PFS_{32}-*b*-$PDMS_{385}$ unimer solution to the samples in (c). Lower-left insets present magnified views of the marked regions, while upper-right insets show photographs of water droplets on the corresponding surfaces together with the measured contact angles (CA). Reproduced from ref. 49 with permission from AAAS, Copyright 2019.

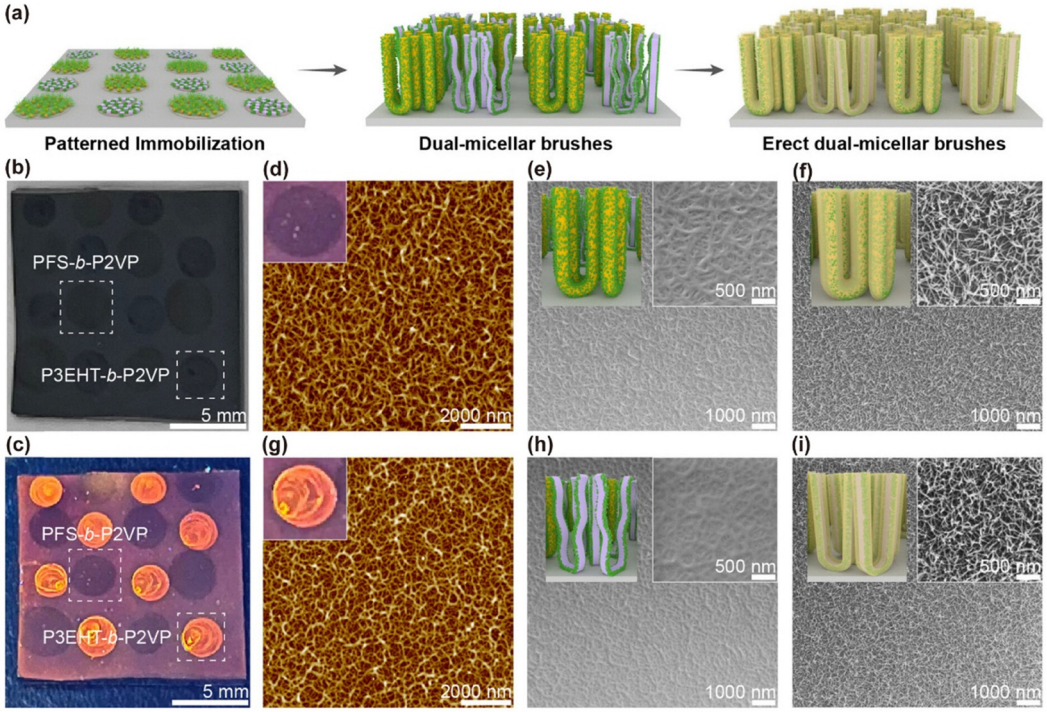

Fig. 11 (a) Schematic showing the fabrication route: patterned immobilization of seed micelles ($P3EHT_{22}$-*b*-$P2VP_{80}$ and PFS_{21}-*b*-$P2VP_{139}$), followed by simultaneous, independent extension of both micellar brush types. Images depict the dual-brush patterns under daylight and UV light, and their subsequent vertical alignment upon Pt nanoparticle loading. (b) and (c) Optical photographs of patterned brushes under daylight (b) and 365 nm UV illumination (c), obtained after adding 3 μL PFS_{21}-*b*-$P2VP_{139}$ unimers and 6 μL $P3EHT_{22}$-*b*-$P2VP_{80}$ unimers (10 mg mL^{-1} in THF each). (d) and (e) AFM (d) and SEM (e) micrographs showing PFS_{21}-*b*-$P2VP_{139}$ brushes confined within the patterned regions. (f) SEM image of vertically aligned PFS_{21}-*b*-$P2VP_{139}$ brushes after treatment with 100 μL Na_2PtCl_6 aqueous solution. (g) and (h) AFM (g) and SEM (h) images displaying patterned $P3EHT_{22}$-*b*-$P2VP_{80}$ brushes. (i) SEM image of their vertical alignment following an identical Pt precursor treatment. Reproduced from ref. 57 with permission from Wiley, copyright 2024.

block chemistries are pre-positioned on a substrate at defined coordinates. Following immobilization, the substrate is exposed to a mixed solution of unimers corresponding to each seed type. Due to selective epitaxial crystallization, each unimer adds exclusively to seeds possessing the same core polymer lattice, preventing cross-nucleation. Zhang *et al.* demonstrated this concept using PFS-based seeds and P3EHT-based seeds patterned on the same substrate. Upon simultaneous addition of their respective unimer feeds, each seed population underwent independent, oriented brush growth, yielding a multi-component micellar brush array in a single reaction step. This approach bypasses the need for sequential deposition, significantly increasing fabrication throughput, and enables the construction of patterned surfaces with spatially encoded chemical, optical, or electronic functionality.

5. Functionalization of micellar brushes

Micellar brushes can act not only as nanoscale templates but also as hierarchically organized functional platforms, either by exploiting the intrinsic physicochemical properties of the constituent block copolymers or by incorporating exogenous functional components. If the block copolymer itself is optoelectronically active, redox-active, semiconducting, or photoreactive, arranging it into a brush architecture can amplify such properties *via* enhanced crystallinity, improved orientational order of functional moieties, and facilitated charge or mass transport. These effects have been demonstrated in contexts such as organic photovoltaics, photoelectrochemical devices, and chemical/biological sensing.

Beyond intrinsic functionality, a wide range of exogenous functionalization strategies can be implemented through chemical handles located in either the corona or the core domain, enabling the immobilization, transformation, or *in situ* generation of new materials without compromising spatial order.

5.1. Corona-mediated conjugation

The solvated corona of surface-immobilized cylindrical micellar brushes offers a highly versatile and accessible binding interface for the incorporation of exogenous functional entities. In particular, P2VP coronas present electron-donating pyridyl nitrogen atoms that are capable of forming stable coordination bonds with a wide range of metal centers. Owing to this property, Sun *et al.* exploited the highly solvated and permeable nature of the P2VP corona to immobilize up to 33 distinct metal species in the form of isolated single atoms, achieving

remarkable loadings in the range of 8.3% to 40.9 wt% (Fig. 12a–d).[53] The forest-like, open three-dimensional architecture of the brushes not only enhanced ion capture efficiency but also promoted rapid mass transport, a feature particularly beneficial during catalytically demanding processes.

In their approach, *in situ* SI-CDSA was performed directly on nickel foam substrates, leading to the growth of PFS-*b*-P2VP brushes. These brushes were subsequently electrostatically complexed with $PtCl_4^{2-}$ ions, which were then stabilized as Pt single-atom "nanoforests" *via* strong coordination to the pyridyl groups in the corona. When the corona is engineered to carry additional charged or polar functional groups, a broader spectrum of noncovalent interactions, such as electrostatics and hydrogen bonding can be exploited for cargo immobilization.

Through these binding pathways, a diverse array of functional materials has been successfully integrated into micellar brush frameworks (Fig. 12e(i)).[51] Examples include MOFs, TiO_2 nanoparticles and enzymes, each imparting distinct physicochemical properties to the hybrid constructs. Such multifunctional architectures exhibit an expanded functional scope, with demonstrated utility in fields as varied as photocatalysis, molecular recognition, and chemical or biological sensing. The combination of structural tunability, high surface accessibility, and adaptable binding chemistry underscores the potential of solvated micellar brushes as a modular platform for advanced hybrid material design.

Beyond simple binding, the structural features of the polymer corona can be rationally exploited to control the spatial

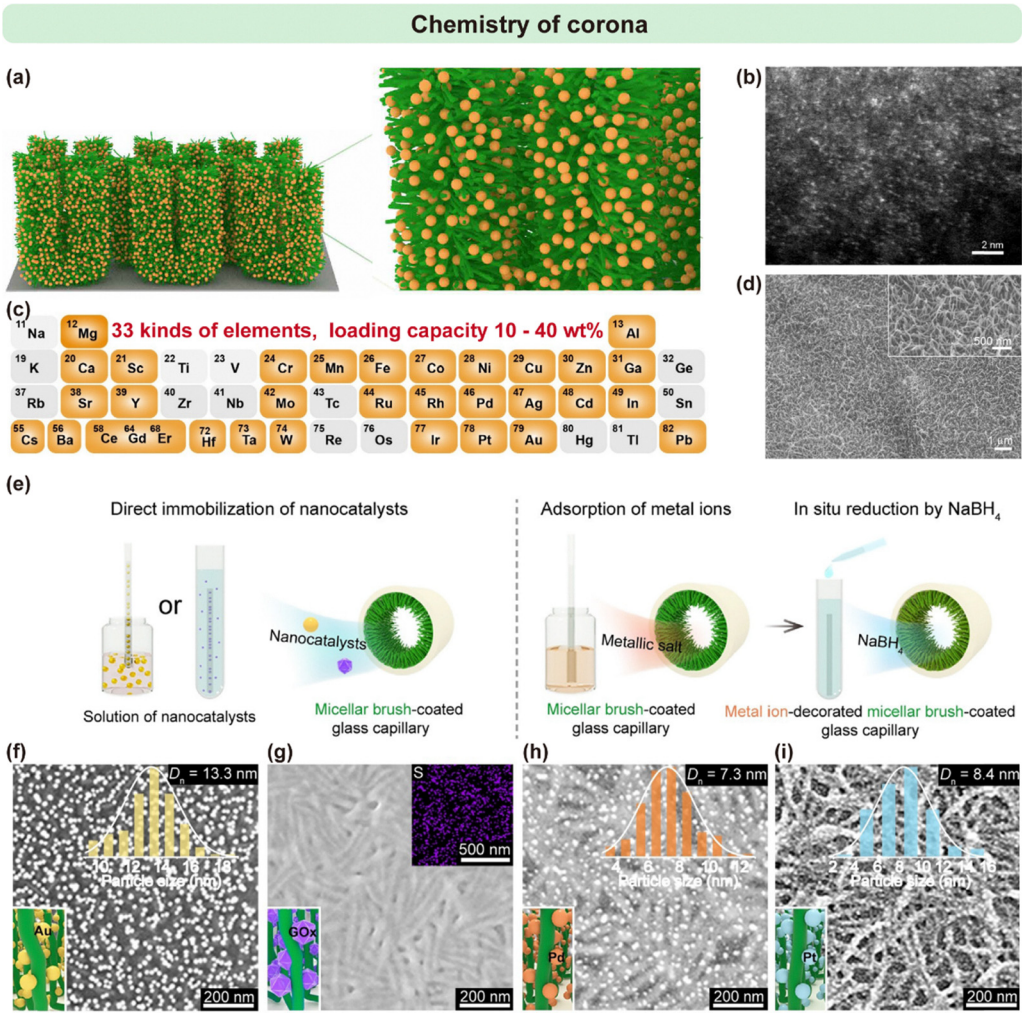

Fig. 12 (a) Schematic representation illustrating the formation of a Pt single-atom nanoforest *via* mild coordination interactions within the micellar brush corona. (b) Aberration-corrected annular dark-field STEM (AC-ADF-STEM) image showing the dispersed Pt single atoms in the nanoforest architecture. (c) Overview of single-atom nanoforests incorporating 32 different metal species. (d) SEM image depicting the surface morphology of the Pt single-atom nanoforest. Reproduced from ref. 53 with permission from AAAS, Copyright 2025. (e) Schematic illustration of two approaches: direct immobilization, in which a solution of the desired nanocatalyst is introduced into a glass capillary coated with PFS_{30}-*b*-$P2VP_{226}$ micellar brushes, allowing spontaneous adsorption *via* coordination, hydrogen bonding, or electrostatic interactions; and *in situ* generation, in which metallic salt and $NaBH_4$ solutions are sequentially introduced by siphoning and soaking. (f) and (g) SEM images of collapsed PFS_{30}-*b*-$P2VP_{226}$ brushes after direct immobilization of (f) Au NPs (inset: Size distribution) and (g) GOx (inset: EDX mapping of sulfur). (h) and (i) SEM images of collapsed brushes after *in situ* generation of (h) Pd NPs and (i) Pt NPs (insets: size distributions). Reproduced from ref. 51 with permission from Wiley, Copyright 2021.

organization and packing density of nanoparticles with nanometer precision. In the work of Tao *et al.*, the well-defined intercoronal spacing of cylindrical PFS-*b*-P2VP micellar brushes (~3.5 nm)[91] was selected to closely match the diameter of pre-synthesized ruthenium nanoparticles (~3.3 nm) (Fig. 13a).[54] This geometric complementarity, combined with the reversible and dynamic nature of Ru–pyridine coordination chemistry, enabled the nanoparticles to infiltrate into the interstitial spaces between P2VP corona chains.

Upon coordination-driven infiltration, local rearrangements of the corona led to a dramatic contraction of the nanoparticle distance from 5.1 ± 1.9 nm in the initial loosely bound state to 0.5 ± 0.08 nm in the final densely packed configuration (Fig. 13b and c). Such close-proximity assembly goes well beyond conventional steric or electrostatic packing, as it requires both spatial matching and dynamic bonding to overcome entropic penalties and corona chain crowding.

The methodology offers several important advantages. First, it allows for collective particle positioning within the polymer template without the need for high-temperature annealing or solvent evaporation-induced aggregation. Second, it enables the translation of nanoscale spatial order into extended, substrate-scale architectures (Fig. 13d and e), manifested in this case as vertically aligned, high-density nanowire arrays of various metals (Ru, Ir, Pt, Rh). By selecting nanoparticles and coronas of appropriate dimensions and coordination chemistries, the approach would be generalized to a broad range of inorganic materials and polymer brush architectures.

In addition, the sub-nanometer interparticle gaps created *via* this strategy are highly relevant for applications in plasmonics,

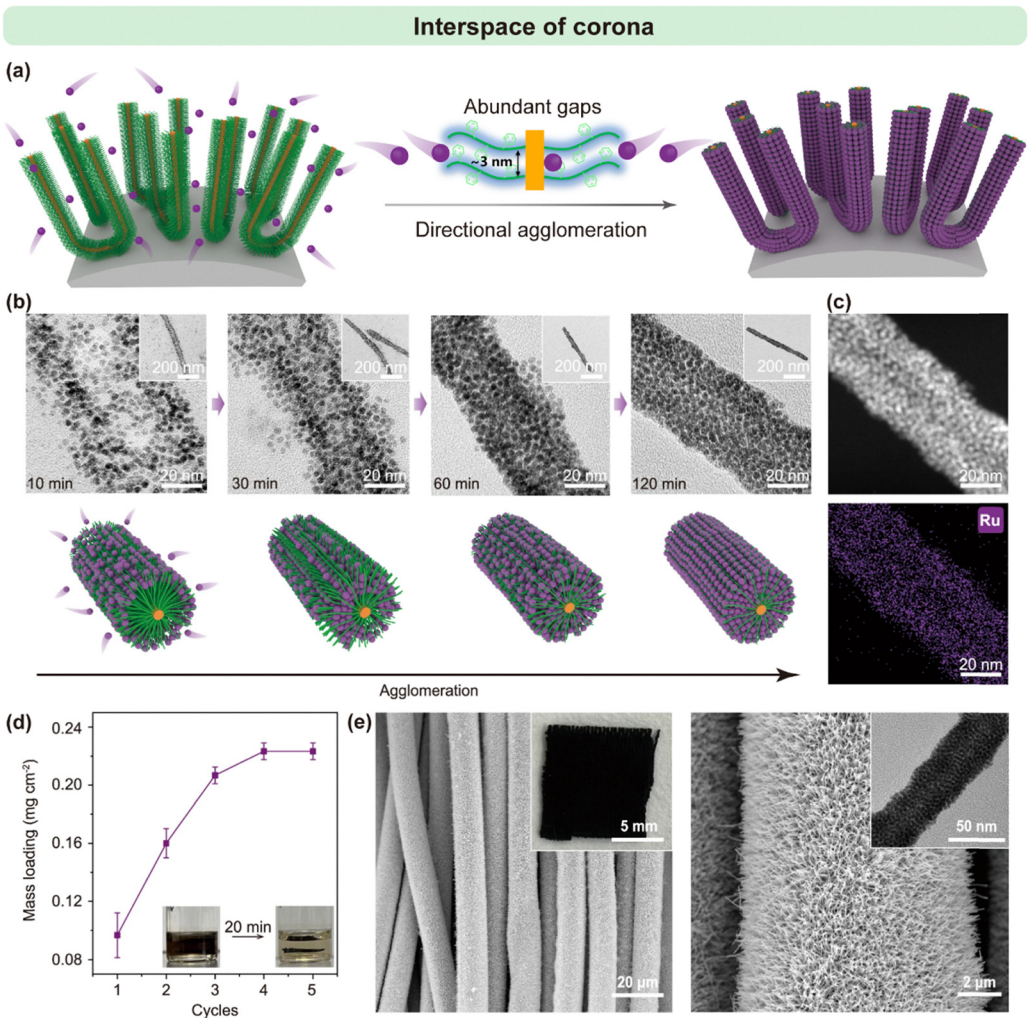

Fig. 13 (a) Schematic representation of the fabrication process for Ru nanoparticle (Ru NP) nanoarrays on carbon cloth. (b) Illustration of Ru NP penetration into the P2VP corona of PFS_{29}-*b*-$P2VP_{230}$ cylindrical micelles, accompanied by TEM images of representative samples at various fabrication stages. (c) High-angle annular dark-field scanning transmission electron microscopy (HAADF-STEM) and energy-dispersive spectroscopy (EDS) mapping of a nanowire densely packed with Ru NPs. (d) Plot showing the dependence of Ru NP mass loading on the number of immersion cycles; inset photographs depict the color change in the Ru NP suspension when micellar brush-modified carbon cloth is introduced. (e) SEM images of Ru NP nanoarrays on carbon cloth. Insets include a photograph of a piece of carbon cloth uniformly coated with the nanoarray and a TEM image of a single nanowire composed of closely stacked Ru NPs. Reproduced from ref. 54 with permission from Spring Nature, copyright 2025.

catalysis, and sensing, where strong near-field coupling or cooperative surface reactions are desired. Control over vertical alignment and periodicity across macroscopic substrates also opens potential pathways toward scalable fabrication of functional nanoscale devices. This study thus demonstrates that the corona is not merely a passive steric barrier, but a tunable, functional scaffold that can mediate structure-specific infiltration and drive the self-organization of nanoparticles into unprecedented dense and ordered arrays.

5.2. Core-driven transformation

The crystalline PFS core within micellar brushes provides a unique reactive scaffold owing to the organometallic nature of its ferrocene units, which exhibit highly reversible Fe(II)/Fe(III) redox chemistry.[93–95] This intrinsic property can be strategically harnessed to *in situ* convert the polymeric core into ordered inorganic nanostructures without disrupting the overall spatial arrangement of the brush array. In the pioneering work of Lu *et al.*,[92] oxidative treatments using strong oxidants such as potassium permanganate ($KMnO_4$), potassium ferrate (K_2FeO_4), dipotassium tetrachloroplatinate (K_2PtCl_4), potassium tetrachloropalladate (K_2PdCl_4), potassium pentachlororuthenate (K_2RuCl_5), gold chloride ($AuCl_3$), and rhodium chloride ($RhCl_3$) were applied to PFS-containing cylindrical micelles anchored on surfaces. During oxidation, the Fe(II) centres in ferrocene are oxidised to Fe(III), triggering cleavage of the Si–C backbone and subsequent precipitation or deposition of the corresponding inorganic species directly within the confinement of the original micellar core domain. The choice of oxidant dictates the chemical identity of the resulting nanostructure: $KMnO_4$ produces well-aligned manganese oxide nanowires (Fig. 14a and b), and noble-metal salts such as $AuCl_3$ can be reduced *in situ* to generate metallic nanoparticles. Importantly, because the transformation proceeds under shape-preserving conditions defined by the crystalline micellar geometry, the resulting inorganic phase inherits the original nanoscale ordering, producing highly uniform, vertically aligned wire- or rod-like arrays (Fig. 14c and d). Such core-to-inorganic conversions open a direct route to integrate functional

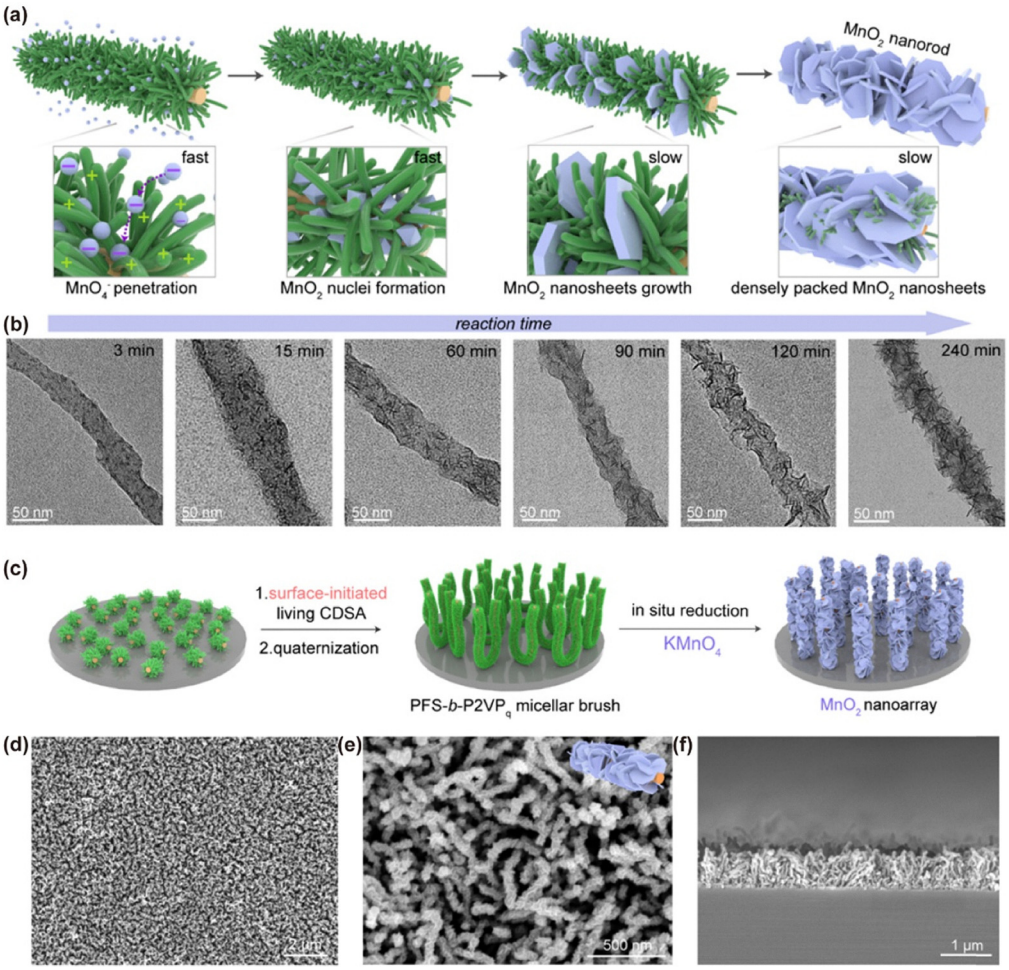

Fig. 14 (a) Schematic illustration of the formation of nanorods densely coated with thin MnO_2 nanosheets *via* a direct redox reaction between PFS-*b*-P2VP$_q$ cylindrical micelles and $KMnO_4$. (b) TEM images depicting the progressive deposition and growth of manganese oxide on PFS-*b*-P2VP$_q$ cylindrical micelles during the redox process. (c) Schematic representation of MnO_2 nanoarray fabrication, involving surface-initiated living growth of PFS-*b*-P2VP$_q$ micellar brushes followed by an *in situ* redox reaction with $KMnO_4$ under ambient conditions. (d, e) Top-view and (f) cross-sectional SEM images of the MnO_2 nanoarray on a silicon wafer. Reproduced from ref. 92 with permission from American Chemical Society, copyright 2025.

metal oxides or noble metals into micellar brush platforms, thereby extending their utility to applications in electrocatalysis, photocatalysis, sensing, and advanced energy-storage systems such as supercapacitors and rechargeable batteries.

5.3. *In situ* transformation and post-assembly processing

After the micellar brush arrays have been immobilized onto a substrate, their exogenous or guest components can be deliberately transformed or modified to access new material phases or functionalities. Such transformations are typically induced by thermal treatment, annealing under controlled atmospheres, or post-assembly chemical reactions, while relying on the pre-organized brush morphology to spatially confine the process and preserve long-range order. This approach enables the conversion from a soft polymeric/scaffolded state into functional inorganic or hybrid nanostructures without sacrificing the nanoscale precision imparted by the original self-assembly.

A representative example was reported by Tao *et al.*, in which metal nanoparticles distributed within the brush framework underwent thermally driven coalescence during high-temperature annealing.[54] At sufficiently elevated temperatures, surface diffusion of the metal atoms caused discrete nanoparticles to merge preferentially along the brush axis, leading to the formation of continuous, nearly single-crystalline metallic nanowires while maintaining their spatial arrangement (Fig. 15a and b). This morphological consolidation had a profound impact on the electronic properties: the direct electrical pathways and reduced grain boundary scattering produced conductivity increases of up to four orders of magnitude compared to the as-prepared state, alongside a marked enhancement of intrinsic metallic behavior (Fig. 15c). By co-incorporating different elemental nanoparticles prior to annealing, Tao and co-workers further demonstrated the fabrication of compositionally controlled alloy nanowire arrays, thereby providing a general route to ordered multimetallic or alloyed architectures at the nanoscale (Fig. 15d and e). Such a strategy holds particular promise for nanoelectronic interconnects, plasmonic waveguides, and catalytically active surfaces.

Thermal treatment can also drive oxidative transformations when performed in ambient air (Fig. 15f–h).[96] In the case of brushes containing metals or metal-ion-loaded cores, controlled thermal oxidation yields ordered arrays of metal-doped metal-oxide nanostructures whose composition, crystallinity, and doping level can be tuned through the precursor loading and annealing profile. This pathway grants access to functional oxides including semiconducting, magnetic, or catalytic variants, whilst retaining the nanoscale order inherited from the micellar template.

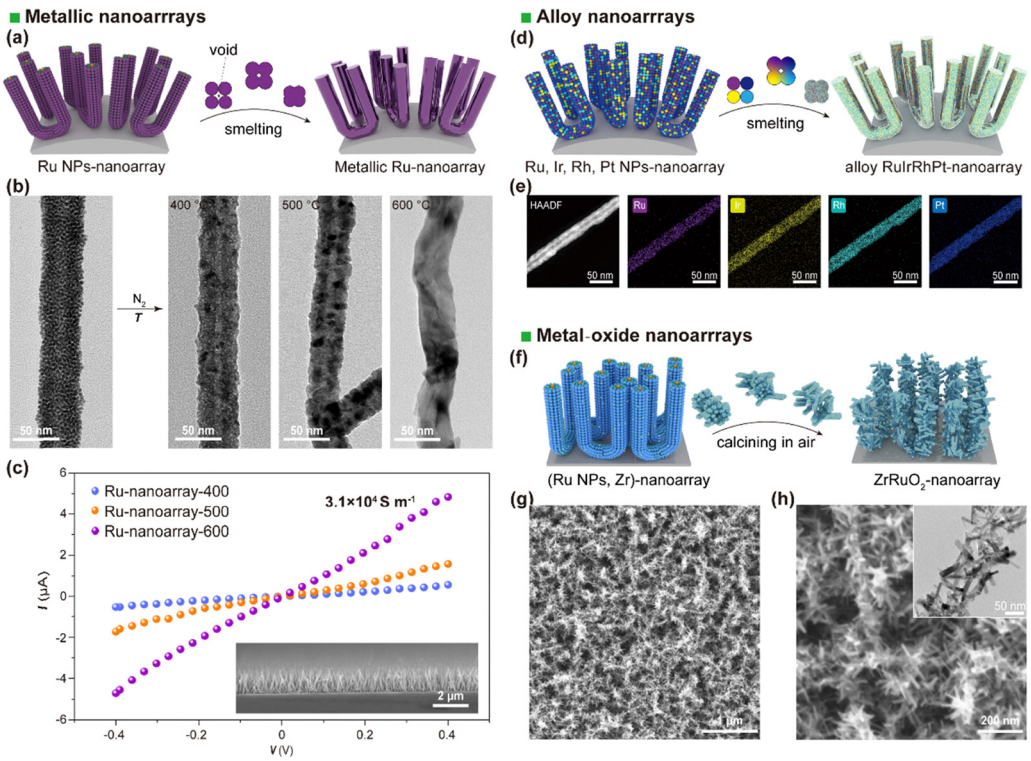

Fig. 15 (a) Schematic representation depicting the transformation of a Ru NP-nanoarray into a continuous metallic Ru nanoarray *via* smelting. (b) TEM images comparing the as-prepared Ru NP-nanoarray with metallic Ru-nanoarrays treated at different temperatures (T = 400, 500, and 600 °C). (c) Electrical conduction measurements of metallic Ru-nanoarray-T. (d) Schematic illustrating the conversion of (Ru, Ir, Rh, Pt) NP-nanoarrays into an alloy RuIrRhPt-nanoarray. (e) HAADF-STEM and EDS elemental mapping images of the alloy nanoarray, showing uniform distributions of Ru, Ir, Rh, and Pt. Reproduced from ref. 54 with permission from Spring Nature, Copyright 2025. (f) Schematic illustrating the fabrication of a $ZrRuO_2$ nanoarray using micellar brushes as a structural template. (g) and (h) SEM images of the $ZrRuO_2$ nanoarray grown on a Ti fiber felt, and TEM image detailing its nanostructure. Reproduced from ref. 96 with permission from Wiley, copyright 2025.

Beyond purely thermal transformations, solution-phase post-assembly reactions have also been harnessed to impart new structural and chemical complexity. As demonstrated by Wang *et al.*, micellar brushes can be sequentially immersed in metal-precursor solutions to load the desired cations into predefined regions, followed by treatment with organic linker solutions under mild conditions (Fig. 16).[97] This stepwise coordination chemistry enables the *in situ* crystallization of MOF nanolayers within or atop the brush-templated sites. The resulting MOF coatings exhibit exceptionally high positional registry and uniform coverage across large substrate areas, demonstrating the ability of the brush scaffold to direct the assembly of porous crystalline materials. Such MOF–polymer hybrid arrays combine the chemical selectivity and sorption capacity of MOFs with the ordered architecture of CDSA-derived brushes, opening avenues in selective sensing, membrane separations, and host–guest catalysis.

By integrating *in situ* phase transformations with the positional fidelity of micellar brush arrays, these post-assembly strategies offer a powerful route to engineer nanoscale materials and heterostructures with precisely orchestrated composition, crystallinity, and functional performance.

6. Applications

The exquisite structural and functional control afforded by SIL-CDSA has positioned it as a compelling platform for a diverse range of applications, from energy conversion and storage to advanced biomedical interfaces and electronic devices.

6.1. Catalytic interfaces

The ability to create high-density, vertically-aligned arrays of nanostructures with high surface area makes SIL-CDSA an ideal method for fabricating advanced catalytic interfaces. The resulting vertically-aligned micellar brush arrays offer a high surface area-to-volume ratio and rationally designed pathways for mass transport, addressing key challenges in heterogeneous catalysis.

6.1.1. Electrocatalytic interface. To solve issues of conventional noble metal powder catalysts (aggregation, poor conductivity, *etc.*), Tao and co-workers used PFS-*b*-P2VP micellar brushes to guide noble metal NPs (Ru, Ir, Rh, Pt) into erect nanoarrays on substrates, then applied high-temperature smelting.[54] Smelting eliminated insulating components, turning NPs into continuous metallic/alloy/metal oxide nanoarrays, boosting electron conductivity by over four orders of magnitude. The resulting interfaces showed excellent performance: metallic Ru-nanoarray-600 (HER) had low overpotential (82.1 mV at 1 A cm^{-2}) and high mass activity (Fig. 17a–c); RuO_x-nanoarray-400 (OER) had 330 mV overpotential at 1 A cm^{-2} and 123× higher mass activity than commercial RuO_2. The PEM electrolyzer with these interfaces ran stably over 500 h at 1 A cm^{-2}, outperforming commercial ones.[54]

6.1.2. Continuous flow catalytic interface. Lin and co-workers developed a versatile catalytic interface on the internal wall of glass capillaries for continuous flow catalysis *via* SIL-CDSA from PFS-*b*-P2VP (Fig. 17d and e).[51] The P2VP corona of these micellar brushes enables flexible decoration of diverse nanocatalysts (*e.g.*, Au, Pd, Pt NPs, TiO_2 NPs, GO_x) through

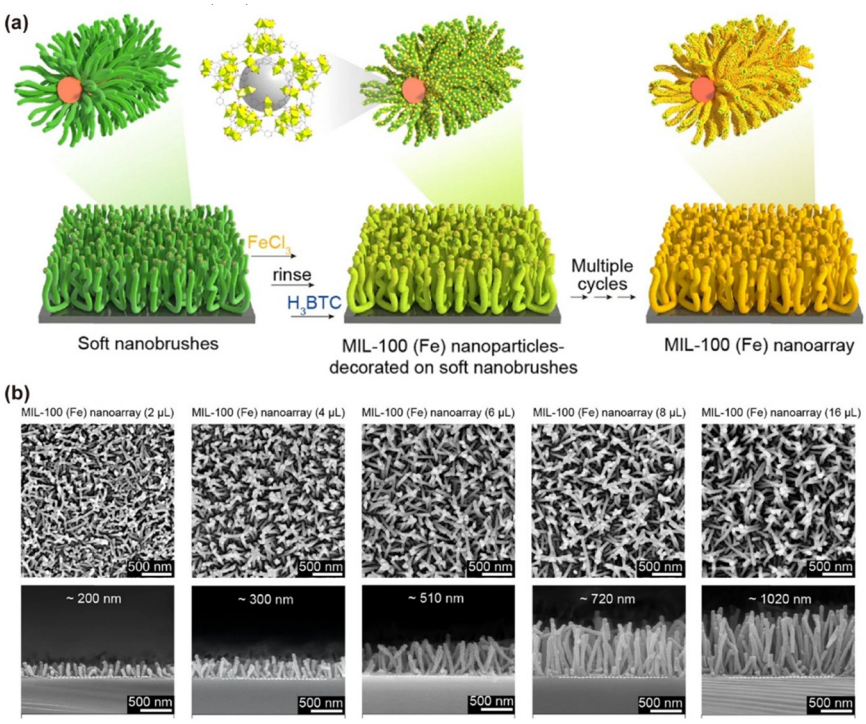

Fig. 16 (a) Schematic representation of the fabrication process for MOF nanoarrays. (b) Top-view and cross-sectional SEM images of MIL-100(Fe) nanoarrays templated by the corresponding soft nanobrushes. Reproduced from ref. 97 with permission from Spring Nature, copyright 2022.

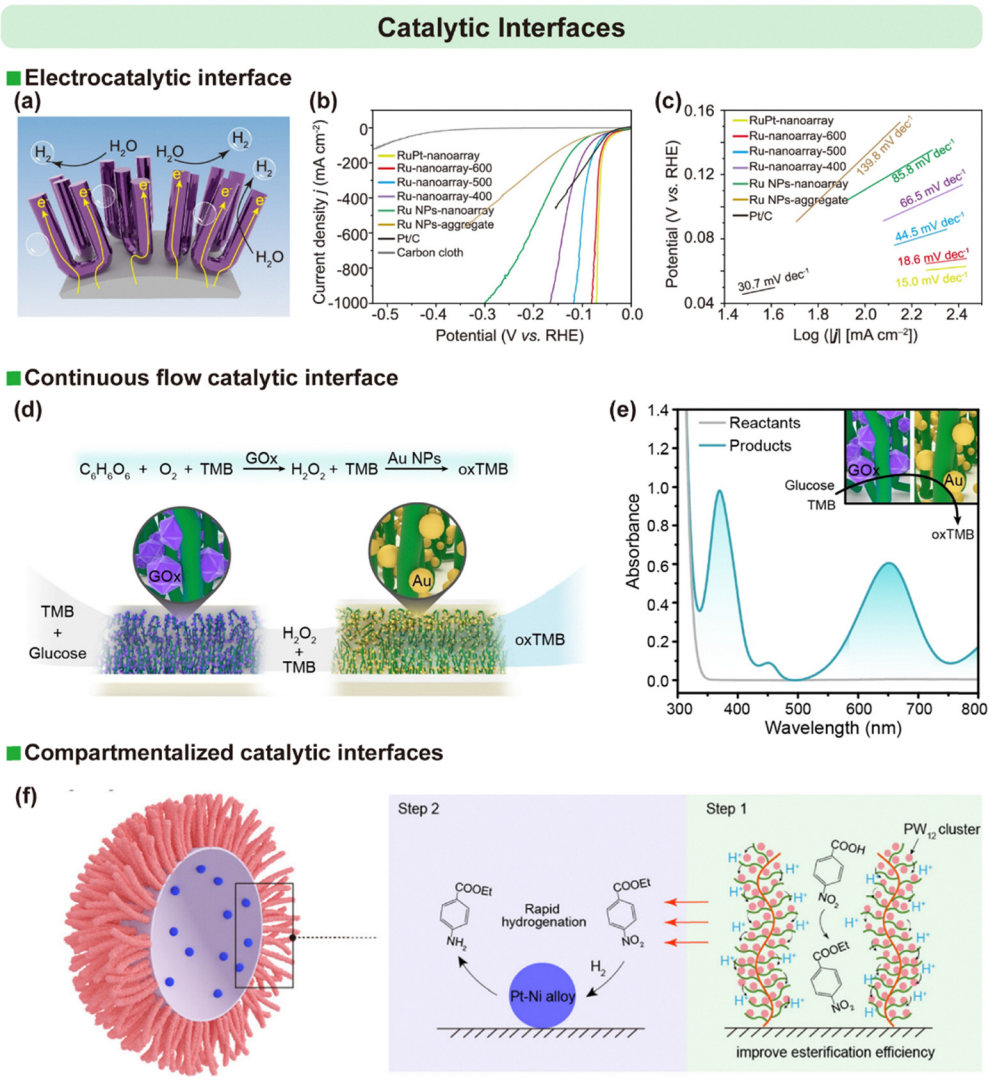

Fig. 17 (a) Schematic representation of a metallic Ru nanoarray designed for the hydrogen evolution reaction (HER). (b) iR-corrected polarization curves in 0.5 M H_2SO_4 solution for alloy RuPt nanoarray, metallic Ru nanoarray-*T*, Ru NP nanoarray, Ru NP aggregates, commercial Pt/C-decorated carbon cloth, and pristine carbon cloth. (c) Tafel plots derived from the polarization curves shown in (b). Reproduced from ref. 54 with permission from Spring Nature, Copyright 2025. (d) and (e) Illustration and UV-vis spectra for a cascade reaction in PBS (pH 5.05) sequentially catalyzed by GOx-functionalized micellar brushes and Au NP-functionalized micellar brushes. Reproduced from ref. 51 with permission from Wiley, copyright 2021. (f) Schematic diagram of the sequential tandem conversion of *p*-nitrobenzoic acid within a microreactor engineered *via* surface modification strategies. Reproduced from ref. 55 with permission from Wiley, copyright 2025.

direct adsorption *via* coordination, H-bonding, or electrostatic interactions or *in situ* growth, forming efficient catalytic interfaces that exhibit excellent activity, stability, and recyclability for various reactions including organic reductions, Suzuki couplings, photodegradations, and multistep cascade reactions.

6.1.3. Compartmentalized catalytic interfaces. From the perspective of micellar brush-directed catalytic interface preparation, high-density PFS-*b*-P2VP micellar brushes are first anchored on the surface of ZIF-8 dodecahedrons *via* SIL-CDSA (Fig. 17f). The P2VP corona then captures functional species (*e.g.*, PW_{12} clusters) to construct external catalytic nanobrushes, while the internal cavity of ZIF-8 (etched to form a hollow structure) encapsulates Pt–Ni alloy nanoparticles. This design enables orthogonal tandem catalysis of *p*-nitrobenzoic acid to benzocaine (95.4% selectivity), where external PW_{12} nanobrushes promote esterification and internal Pt–Ni alloys drive hydrogenation, with spatial isolation optimizing reaction kinetics and suppressing cross-reaction.

6.2. Bioinspired interfaces

Micellar brushes are employed as core templates to engineer bioinspired interfaces for high-performance piezoresistive electronic skins (E-skins), effectively addressing the challenge of fabricating well-defined nanostructures on soft substrates under mild processing conditions.[52] To prepare the substrate, PDMS–CB films featuring micrometer-scale wavy surfaces were obtained by casting a PDMS/CB mixture onto sandpaper molds,

followed by thermal curing (Fig. 18a). The microdome dimensions within the PDMS–CB films were precisely tuned by selecting sandpaper with mesh sizes ranging from 200 to 1000. Subsequently, micelle seeds were uniformly deposited across the PDMS–CB surface. Due to their nanoscale size, the seeds were able to conformally coat the irregular topography, enabling the growth of a dense micellar brush upon addition of PFS_{32}-*b*-$P2VP_{251}$ unimers. Platinum nanoparticle (Pt NP)–based nanoarrays were then formed *via in situ* aggregation within the micellar domains, leading to large-area hierarchical architectures after freeze-drying (Fig. 18b).

The resulting E-skins, incorporating these hierarchical structures, were assessed for their piezoresistive performance under applied pressures from 0 to 200 kPa. Devices with the smallest microdome features (1000- and 800-mesh) exhibited a characteristic two-stage increase in relative current change, with a limited linear sensing range. Increasing the microdome size (600–200 mesh) significantly enhanced linearity, with the E-skin fabricated from 600-mesh sandpaper achieving an outstanding linear response across the entire 0.1–200 kPa range and an impressive sensitivity of 110.05% kPa^{-1} (Fig. 18c).

To further validate the linear pressure detection capability, a sequence of static weights was applied individually to the surface of the hierarchically structured E-skin. The relative current varied linearly with increasing pressure in the 0.5–50 kPa range (Fig. 18d). Under a high base load of 50 kPa, the device was able to resolve successive 2 kPa increments with remarkable precision (Fig. 18e). Additionally, when immersed at various depths in water, the sensor accurately detected hydrostatic pressure variations (Fig. 18f). This combination of broad-range linearity, high sensitivity, and excellent resolution highlights the potential of such hierarchical E-skins for wearable sensing systems in next-generation aquatic or snorkeling applications.

6.3. Devices

The integration of SIL-CDSA architectures into functional devices is a rapidly advancing frontier. The oriented nature of the nanostructures is particularly beneficial for charge-based devices. Tao *et al.* applied SIL-CDSA to fabricate ruthenium-containing nanowire brush arrays directly on PEM for electrolytic water splitting (Fig. 19a and b).[54,96] The oriented, high-surface-area

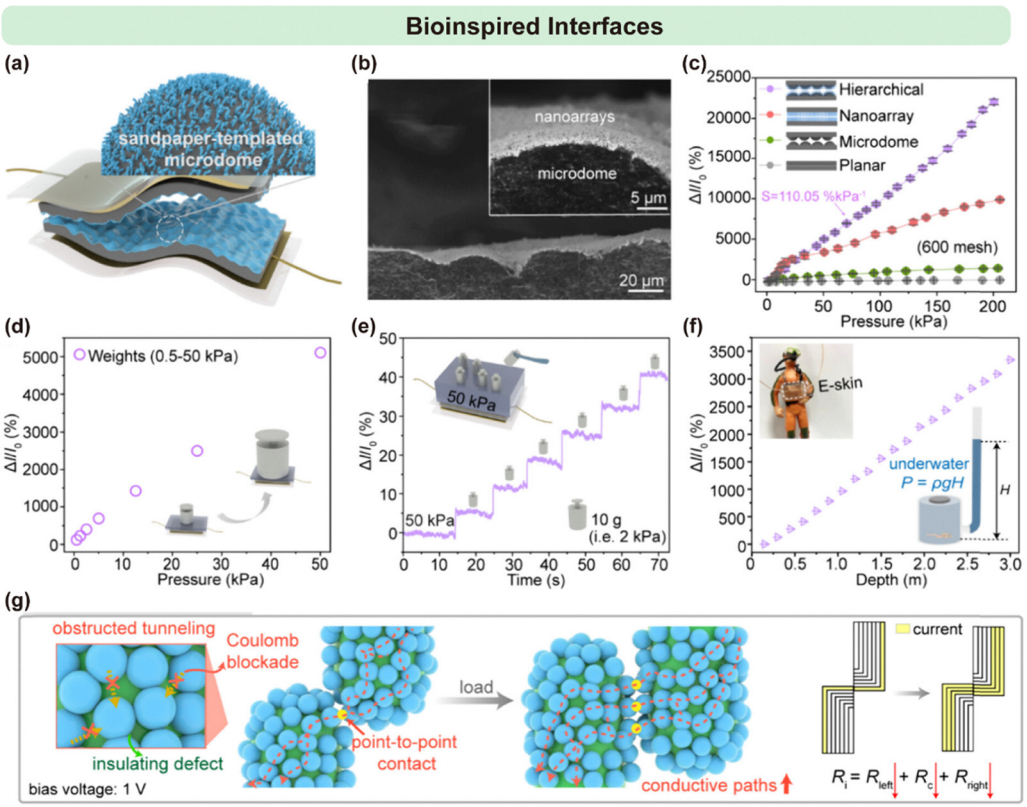

Fig. 18 (a) Schematic representation of a hierarchically structured electronic skin (E-skin) featuring micelle/Pt nanoarrays on the surface of a microdome-patterned PDMS–CB film. (b) Cross-sectional SEM images of the hierarchically structured film prepared using 600-mesh sandpaper. (c) Relative current variations for different E-skin configurations within 200 kPa pressure range. Bias voltage = 1 V. (d) Static weight pressure sensing at applied pressures of 0.5, 1.25, 2.5, 5, 12.5, 25, and 50 kPa. (e) Detection of an additional small pressure of 2 kPa (weight: 10 g, applied area: 5×10^{-5} m^2) under a preload pressure of 50 kPa (weight: 250 g, applied area: 5×10^{-5} m^2). (f) Relative current change of the hierarchically structured E-skin under varying water levels. Inset: schematic diagram illustrating hydrostatic pressure detection. (g) Schematic illustrating electron transport and conductive pathways during loading between a pair of interlocked micelle/Pt nanoarrays composed of various nanoparticles. R_i: total resistance of the interlocked nanoarrays under load; R_{left} and R_{right}: internal resistances of each nanoarray; R_c: contact resistance. Reproduced from ref. 52 with permission from American Chemical Society, copyright 2025.

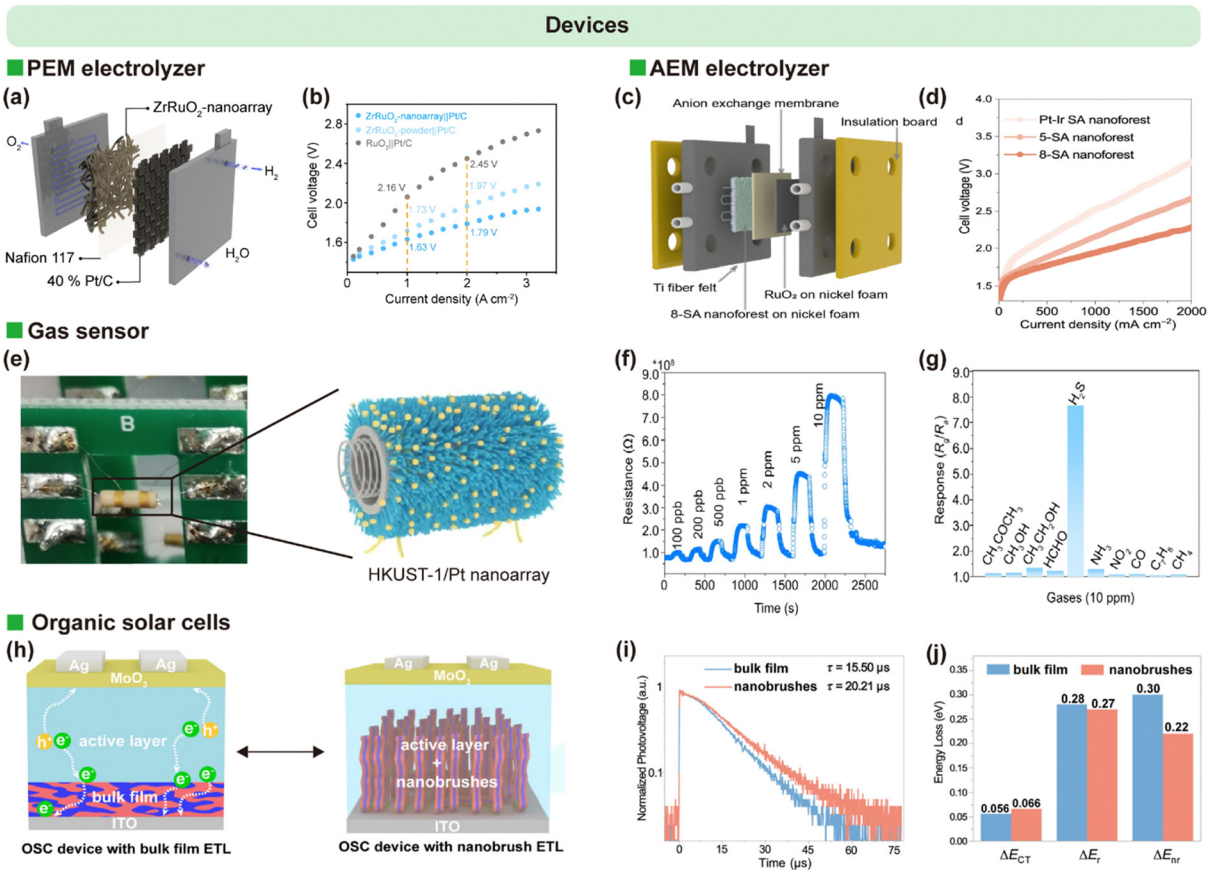

Fig. 19 (a) Schematic diagram of a PEM electrolyzer. (b) Current–voltage (*I*–*V*) curves of electrolyzers employing $ZrRuO_2$ nanoarray, $ZrRuO_2$ powder, and commercial RuO_2 as the anode, respectively. Reproduced from ref. 54 with permission from Spring Nature, Copyright 2025. (c) Schematic illustration of the AEM electrolyzer device. (d) *I*–*V* curves of the AEM electrolyzer using Pt–Ir SA, 5-SA, and 8-SA nanoforests as the cathodic catalyst and commercial RuO_2 as the anodic catalyst at 60 °C. Reproduced from ref. 53 with permission from AAAS, Copyright 2025. (e) Schematic of a side-heated HKUST-1 nanoarray-based gas sensor. (f) Response–recovery curves of the HKUST-1 nanoarray/Pt-0.36 sensor to H_2S at various concentrations at 200 °C. (g) Responses of the HKUST-1 nanoarray/Pt-0.36 sensor to different chemical vapors (10 ppm) at 200 °C. Reproduced from ref. 97 with permission from Spring Nature, Copyright 2022. (h) Schematic illustration of charge transport in inverted organic solar cells (OSCs) based on bulk films and nanobrushes. (i) Transient photovoltage decay curves of bulk film–based and nanobrush–based OSCs. (j) Detailed energy loss analysis in bulk film–based and nanobrush–based OSCs. Reproduced from ref. 56 with permission from American Chemical Society, Copyright 2025.

arrangement facilitated efficient proton conduction and catalytic exposure, improving the performance of PEM electrolyzers. Similarly, Sun *et al.* developed dense "nanoforests" of cylindrical micellar brushes as electrode interfaces in AEM electrolyzers (Fig. 19c and d).[53] By tailoring the corona chemistry to promote hydroxide ion transport and catalyst dispersion, these vertically aligned structures enhanced reaction kinetics and reduced polarization losses.

Wang *et al.* exploited SIL-CDSA to grow MOF arrays on the surface of ceramic tubes (Fig. 19e–g).[97] The oriented MOF coating provided uniform pore channels and high accessible surface area, enabling sensitive and selective gas detection with rapid response times. Yang *et al.* employed fully conjugated PF-*b*-QPT micellar brushes as structurally ordered, photoactive interlayers in organic solar cells (Fig. 19h–j).[56] The brush orientation promoted directional charge transport, while the conjugated corona improved light absorption and exciton dissociation, resulting in enhanced power conversion efficiency relative to disordered control layers.

These examples collectively illustrate the versatility of SIL-CDSA in device engineering: the method offers nanostructural precision, orientation control, and compositional diversity in a single platform. Continued development of this approach is expected to open pathways to high-performance systems across energy conversion, sensing, and optoelectronic technologies.

7. Conclusion and perspectives

Surface-initiated living crystallization-driven self-assembly (SIL-CDSA) has evolved rapidly from a nascent concept into a robust and versatile strategy for precision nanofabrication on surfaces. As outlined in this review, the field has made significant advances in controlling the dimensions, morphology, and functionality of surface-grafted nanostructures. The ability to produce dense, vertically aligned arrays of micelles and platelets with tunable height, width, and area has provided unprecedented architectural control. Complex structures such as

asymmetric platelets and patterned hierarchical assemblies, have been realized alongside the programmed integration of multi-component systems. By harnessing both intrinsic polymer functionalities and post-assembly modification of the micellar corona, these architectures have found application in catalysis, electronics, and biomedicine. Landmark achievements, including the fabrication of patterned dual-micellar brushes, and the construction of high-performance electrodes and microreactors, highlight the transformative potential of this bottom-up approach for next-generation materials and devices.

Despite this progress, several fundamental challenges and exciting opportunities remain, which will define the future trajectory of the field.

1. Expanding the materials library: a significant portion of seminal SIL-CDSA work has relied on a relatively small set of well-behaved, crystallizable BCPs, most notably those based on PFS. While systems based on conjugated polymers like P3EHT and PF are emerging, there is a critical need to expand the library of materials amenable to SIL-CDSA. This involves designing new BCPs with diverse crystallizable cores (*e.g.*, biodegradable polyesters, high-performance engineering polymers) and functional coronas. Success here will broaden the application space to areas like transient electronics and high-temperature materials.

2. Deepening mechanistic understanding: while the general principles of SIL-CDSA are understood, a deeper, quantitative understanding of the kinetics and thermodynamics at the solid–liquid interface is needed. How does the chemical and physical nature of the substrate (*e.g.*, hydrophobicity, surface energy, crystallinity) precisely influence unimer diffusion, epitaxial addition rates, and the stability of the resulting structures? Advanced *in situ* characterization techniques, such as liquid-cell atomic force microscopy and surface-sensitive scattering methods, combined with sophisticated computational modeling, will be essential to unravel these complex interactions and develop predictive models for SIL-CDSA.

3. Achieving true three-dimensional complexity: current SIL-CDSA methods excel at creating dense 2.5D structures—essentially extruded 2D patterns. The next grand challenge is to achieve true 3D architectural control, enabling the fabrication of structures with programmed complexity not just on the surface but in the vertical dimension as well. This might involve techniques that can switch growth direction, alternate between 1D and 2D growth modes, or integrate orthogonal self-assembly processes. The CDSA-PISA concept is a step in this direction, but realizing complex, interconnected 3D networks remain an open frontier.

4. Scalability and manufacturing: to move from the laboratory to industrial application, fabrication methods must be scalable, cost-effective, and compatible with existing manufacturing platforms. While flow-based synthesis and rapid self-assembly protocols are promising, significant work is needed to translate the precise, multi-step process of seed immobilization and growth to large-area substrates (*e.g.*, wafer-scale). Developing parallel, high-throughput techniques for surface patterning and growth will be paramount for the technological maturation of SIL-CDSA.

In conclusion, SIL-CDSA stands at a pivotal juncture. It has firmly established its credentials as a premier tool for bottom-up nanofabrication on surfaces. The future of the field lies in diversifying its material palette, deepening its mechanistic foundations, elevating its architectural complexity into the third dimension, and engineering scalable pathways to manufacturing. By addressing these challenges, SIL-CDSA is poised to deliver a new generation of smart, functional interfaces that will drive innovation across science and technology.

Author contributions

Jiawei Tao: conceptualization, writing – original draft; Chenchen Gao, Yao Lu: writing – original draft; Zhenyan Ji, Peiwen Wang, Sen Lv, Xiaomin Cai, Jingwen Zhang: writing – review & editing; Huibin Qiu: conceptualization, funding acquisition, supervision, writing – review & editing.

Conflicts of interest

There are no conflicts to declare.

Data availability

No primary research results, software or code have been included and no new data was generated or analyzed as part of this review.

Acknowledgements

This work was financially supported by the National Natural Science Foundation of China (22425203, 52403329, 22561160131), the Innovation Program of Shanghai Municipal Education Commission (202101070002E00084) and the Natural Science Foundation of Shanghai (25ZR1402249).

Notes and references

1 P. Zhang, X. Wang, Y. Zhang, Y. Wei, N. Shen, S. Chen and B. Xu, *Adv. Funct. Mater.*, 2024, **34**, 2402307.
2 C. Liu, H. Ma, S. Yuan, Y. Jin and W. Tian, *ACS Nano*, 2025, **19**, 2047–2069.
3 L. Ma and H. Yang, *Bio-Des. Manuf.*, 2023, **6**, 735–741.
4 J. Cai, C. Li and I. Manners, *Angew. Chem., Int. Ed.*, 2025, **64**, e202501552.
5 L. Xiao, T. Xia, J. Zhang, S. J. Parkinson, J. Y. Rho, A. P. Dove and R. K. O'. Reilly, *Nat. Synth.*, 2025, **4**, 808–815.
6 N. R. Glavin, P. M. Ajayan and S. Kar, *Adv. Mater.*, 2023, **35**, 2204928.
7 C. Mao, *Adv. Mater.*, 2025, **37**, 2418618.
8 S. Park, S.-Y. Kang, S. Yang and T.-L. Choi, *J. Am. Chem. Soc.*, 2024, **146**, 19369–19376.

9 F. A. Escobedo, A. Haji-Akbari and S. Sharma, *J. Chem. Theory Comput.*, 2024, **20**, 1503–1504.
10 S.-H. Yu, R. O'Reilly, L. Jiang and N. A. Kotov, *Acc. Chem. Res.*, 2022, **55**, 1783–1784.
11 Y. Song, *Nat. Chem. Biol.*, 2024, **20**, 1549.
12 J. Cornel Erik, J. Jiang, S. Chen and J. Du, *CCS Chem*, 2020, **3**, 2104–2125.
13 S. Pearce, H. K. MacKenzie, H. Shaikh, Z. Liu, R. Harniman, J. C. Eloi, S. Davis, R. M. Richardson, E. A. LaPierre, I. Manners and Y. Zhang, *Angew. Chem., Int. Ed.*, 2025, **64**, e202506872.
14 J. Zhang, T. Xiao, Z. Liu, Y. Yin, C. Li, F. Xu and Y. Mai, *J. Am. Chem. Soc.*, 2025, **147**, 19148–19156.
15 R. A. Scanga, A. Shahrokhinia, J. Borges, S. H. Sarault, M. B. Ross and J. F. Reuther, *J. Am. Chem. Soc.*, 2023, **145**, 6319–6329.
16 J. Gu, Z. Chu, B. Zheng and Z. Tong, *ACS Macro Lett.*, 2025, **14**, 645–657.
17 J. Jiang and M. A. Winnik, *Acc. Chem. Res.*, 2025, **58**, 1683–1695.
18 S. Mahapatra, P. Dey and G. Ghosh, *Polym. J.*, 2024, **56**, 949–975.
19 A. Sahu, S. Mahapatra, P. Dey and G. Ghosh, *Macromol. Chem. Phys.*, 2025, **226**, 2400426.
20 Y. Guo, T. Xia, V. Walter, Y. Xie, J. Y. Rho, L. Xiao, R. K. O'Reilly and M. I. Wallace, *Nat. Commun.*, 2025, **16**, 2672.
21 T. Xia, L. Xiao, Y. Xie, A. P. Dove and R. K. O'Reilly, *Chem. Rev.*, 2025, **125**, 10105–10178.
22 L. Liu, L. Zhu, Z. Chu and Z. Tong, *Macromolecules*, 2023, **56**, 5984–5992.
23 L. Zhu, L. Liu, S. Varlas, R.-Y. Wang, R. K. O'Reilly and Z. Tong, *ACS Nano*, 2023, **17**, 24141–24153.
24 H. Qiu, G. Russo, P. A. Rupar, L. Chabanne, M. A. Winnik and I. Manners, *Angew. Chem., Int. Ed.*, 2012, **51**, 11882–11885.
25 Z. Deng, Y. Sun, Z. Chen, Y. Zhao and A. Chen, *Macromolecules*, 2025, **58**, 2345–2356.
26 J. Nie, J. Zhao, L. Li, T. Zhou and G. Guerin, *Angew. Chem., Int. Ed.*, 2025, **64**, e202511515.
27 Y.-N. Pan, C.-C. Ye, S.-L. Huang, C. Wang, M.-Y. Han and L. Xu, *Angew. Chem., Int. Ed.*, 2025, **64**, e202418131.
28 Y. Gao, H. Qiu, H. Zhou, X. Li, R. Harniman, M. A. Winnik and I. Manners, *J. Am. Chem. Soc.*, 2015, **137**, 2203–2206.
29 J. Nie, Z. Wang, L. Xia, X. Huang, G. Lu and C. Feng, *Eur. Polym. J.*, 2023, **197**, 112384.
30 J. R. Finnegan, D. J. Lunn, O. E. C. Gould, Z. M. Hudson, G. R. Whittell, M. A. Winnik and I. Manners, *J. Am. Chem. Soc.*, 2014, **136**, 13835–13844.
31 F. Teng, B. Xiang, L. Liu, S. Varlas and Z. Tong, *J. Am. Chem. Soc.*, 2023, **145**, 28049–28060.
32 Z. Tong, Y. Xie, M. C. Arno, Y. Zhang, I. Manners, R. K. O'Reilly and A. P. Dove, *Nat. Chem.*, 2023, **15**, 824–831.
33 H. Qiu, Y. Gao, C. E. Boott, O. E. C. Gould, R. L. Harniman, M. J. Miles, S. E. D. Webb, M. A. Winnik and I. Manners, *Science*, 2016, **352**, 697–701.
34 R. Deng, X. Mao, S. Pearce, J. Tian, Y. Zhang and I. Manners, *J. Am. Chem. Soc.*, 2022, **144**, 19051–19059.
35 A. Nazemi, X. He, L. R. MacFarlane, R. L. Harniman, M.-S. Hsiao, M. A. Winnik, C. F. J. Faul and I. Manners, *J. Am. Chem. Soc.*, 2017, **139**, 4409–4417.
36 Y. Su, Y. Jiang, L. Liu, Y. Xie, S. Chen, Y. Wang, R. K. O'Reilly and Z. Tong, *Macromolecules*, 2022, **55**, 1067–1076.
37 T. Xia, L. Xiao, K. Sun, J. Y. Rho, Y. Xie, S. J. Parkinson, L. Sangroniz, J. Zhang, J. Lin, A. J. Müller, L. Gao, A. P. Dove and R. K. O'Reilly, *Macromolecules*, 2024, **57**, 11210–11220.
38 F. Teng, J. Gu, Z. Chu and Z. Tong, *Macromolecules*, 2025, **58**, 249–255.
39 Z. M. Hudson, C. E. Boott, M. E. Robinson, P. A. Rupar, M. A. Winnik and I. Manners, *Nat. Chem.*, 2014, **6**, 893–898.
40 H. Qiu, Z. M. Hudson, M. A. Winnik and I. Manners, *Science*, 2015, **347**, 1329–1332.
41 X. Li, Y. Gao, C. E. Boott, D. W. Hayward, R. Harniman, G. R. Whittell, R. M. Richardson, M. A. Winnik and I. Manners, *J. Am. Chem. Soc.*, 2016, **138**, 4087–4095.
42 X. Li, Y. Gao, C. E. Boott, M. A. Winnik and I. Manners, *Nat. Commun.*, 2015, **6**, 8127.
43 X. Li, Y. Gao, R. Harniman, M. Winnik and I. Manners, *J. Am. Chem. Soc.*, 2016, **138**, 12902–12912.
44 H. K. MacKenzie, Y. Zhang, W. Zheng, H. Shaikh, L. R. MacFarlane, R. A. Musgrave and I. Manners, *J. Am. Chem. Soc.*, 2024, **146**, 18504–18512.
45 B. Jin, Q. Li, L. Hu, Q. Liu, Y. Chen, Y. Luo, S. Chi and X. Li, *Angew. Chem., Int. Ed.*, 2023, **62**, e202219067.
46 C. Zhang, J. Lin, L. Wang and L. Gao, *J. Phys. Chem. Lett.*, 2022, **13**, 6215–6222.
47 X. Wang, K. Liu, A. C. Arsenault, D. A. Rider, G. A. Ozin, M. A. Winnik and I. Manners, *J. Am. Chem. Soc.*, 2007, **129**, 5630–5639.
48 J. Feng, Y. Qiu, H. Gao and Y. Wu, *Acc. Chem. Res.*, 2024, **57**, 222–233.
49 J. Cai, C. Li, N. Kong, Y. Lu, G. Lin, X. Wang, Y. Yao, I. Manners and H. Qiu, *Science*, 2019, **366**, 1095–1098.
50 T. Gädt, N. S. Ieong, G. Cambridge, M. A. Winnik and I. Manners, *Nat. Mater.*, 2009, **8**, 144–150.
51 G. Lin, J. Cai, Y. Sun, Y. Cui, Q. Liu, I. Manners and H. Qiu, *Angew. Chem., Int. Ed.*, 2021, **60**, 24637–24643.
52 Y. Lu, Y. Xing, J. Tao, S. Wang, G. Lin, H. Zhang and H. Qiu, *Chem. Mater.*, 2025, **37**, 3274–3283.
53 Y. Sun, Y. Zang, B. He, G. Lin, Z. Liu, L. Yang, L. Chen, L. Li, X. Liu, C. Shen and H. Qiu, *Sci. Adv.*, 2025, **11**, eadq2948.
54 J. Tao, R. Gao, G. Lin, C. Chu, Y. Sun, C. Yu, Y. Ma and H. Qiu, *Nat. Commun.*, 2025, **16**, 4996.
55 S. Wang, Y. Wang, B. Fang, S. Zhang, H. Zhou, Y. Lu, C. Shen and H. Qiu, *Angew. Chem., Int. Ed.*, 2025, **64**, e202508249.
56 L. Yang, C. Li, N. An, J. Gao, Y. Wei, J. Qiao, J. Dai, N. Yu, Y. Sun, Q. Lin, X. Zhang, J. Zhang, Z. Tang, X. Hao, G. Lu, Z. Wei, I. Manners, Y. Kuang, H. Huang, A. Facchetti and H. Qiu, *J. Am. Chem. Soc.*, 2025, **147**, 6763–6771.
57 Y. Zhang, L. Yang, Y. Sun, G. Lin, I. Manners and H. Qiu, *Angew. Chem., Int. Ed.*, 2024, **63**, e202315740.

58 R. L. Harniman, S. Pearce and I. Manners, *J. Am. Chem. Soc.*, 2022, **144**, 951–962.
59 Z. Sun, Z. Xu, M. Ding, L. Wang, L. Zhao, P. Sui, G. Li, H. Jin, Y. Zhou and S. Lin, *Angew. Chem., Int. Ed.*, 2025, **64**, e202503104.
60 J. Tan, J. Zhang, M. Chen, J. Cen, W. Wang, C. You, X. Hu, J. Hu and S. Liu, *Angew. Chem., Int. Ed.*, 2025, e22563.
61 Z. Li, S. Wang, Y. Ma, J. C. M. van Hest and H. Che, *Angew. Chem., Int. Ed.*, 2025, e22097.
62 J. Xiao and J. Du, *J. Am. Chem. Soc.*, 2020, **142**, 6569–6577.
63 T. Wang, Y. Li, E. J. Cornel, C. Li and J. Du, *ACS Nano*, 2021, **15**, 9027–9038.
64 E. Equy, E. Ibarboure, E. Grelet and S. Lecommandoux, *J. Am. Chem. Soc.*, 2025, **147**, 9727–9738.
65 Z. Sun, Z. Xu, P. Wu, L. Wang, M. Ding, L. Zhao, Y. Zheng, Y. Zhou, S. Lin and H. Jin, *Angew. Chem., Int. Ed.*, 2025, **64**, e202507852.
66 Y. Luo, H. Wu, X. Zhou, J. Wang, S. Er, Y. Li, P. L. W. Welzen, R. A. J. F. Oerlemans, L. K. E. A. Abdelmohsen, J. Shao and J. C. M. van Hest, *J. Am. Chem. Soc.*, 2023, **145**, 20073–20080.
67 M.-Y. Li, L.-M. Wu, H.-Q. Xie and B. Shen, *Sci. Adv.*, 2025, **11**, eadv8999.
68 Y. Cha, C. Jarrett-Wilkins, M. A. Rahman, T. Zhu, Y. Sha, I. Manners and C. Tang, *ACS Macro Lett.*, 2019, **8**, 835–840.
69 J. B. Gilroy, D. J. Lunn, S. K. Patra, G. R. Whittell, M. A. Winnik and I. Manners, *Macromolecules*, 2012, **45**, 5806–5815.
70 Y. Zhang, S. Pearce, J.-C. Eloi, R. L. Harniman, J. Tian, C. Cordoba, Y. Kang, T. Fukui, H. Qiu, A. Blackburn, R. M. Richardson and I. Manners, *J. Am. Chem. Soc.*, 2021, **143**, 5805–5814.
71 T. Xia, Z. Tong, Y. Xie, M. C. Arno, S. Lei, L. Xiao, J. Y. Rho, C. T. J. Ferguson, I. Manners, A. P. Dove and R. K. O'Reilly, *J. Am. Chem. Soc.*, 2023, **145**, 25274–25282.
72 J. Qian, Y. Lu, G. Cambridge, G. Guerin, I. Manners and M. A. Winnik, *Macromolecules*, 2012, **45**, 8363–8372.
73 S. Ganda and M. H. Stenzel, *Prog. Polym. Sci.*, 2020, **101**, 101195.
74 J. Qian, G. Guerin, Y. Lu, G. Cambridge, I. Manners and M. A. Winnik, *Angew. Chem., Int. Ed.*, 2011, **50**, 1622–1625.
75 G. Guerin, G. Molev, P. A. Rupar, I. Manners and M. A. Winnik, *Macromolecules*, 2020, **53**, 10198–10211.
76 X. Wang, G. Guerin, H. Wang, Y. Wang, I. Manners and M. A. Winnik, *Science*, 2007, **317**, 644–647.
77 S. K. Patra, R. Ahmed, G. R. Whittell, D. J. Lunn, E. L. Dunphy, M. A. Winnik and I. Manners, *J. Am. Chem. Soc.*, 2011, **133**, 8842–8845.
78 J. Gwyther, J. B. Gilroy, P. A. Rupar, D. J. Lunn, E. Kynaston, S. K. Patra, G. R. Whittell, M. A. Winnik and I. Manners, *Chem. – Eur. J.*, 2013, **19**, 9186–9197.
79 J. Qian, X. Li, D. J. Lunn, J. Gwyther, Z. M. Hudson, E. Kynaston, P. A. Rupar, M. A. Winnik and I. Manners, *J. Am. Chem. Soc.*, 2014, **136**, 4121–4124.
80 W. Yu, M. Inam, J. R. Jones, A. P. Dove and R. K. O'Reilly, *Polym. Chem.*, 2017, **8**, 5504–5512.
81 Y. He, J.-C. Eloi, R. L. Harniman, R. M. Richardson, G. R. Whittell, R. T. Mathers, A. P. Dove, R. K. O'Reilly and I. Manners, *J. Am. Chem. Soc.*, 2019, **141**, 19088–19098.
82 J. H. Hwang, J. Yoon, M. Seo, J. P. Patterson and E. Lee, *Matter*, 2025, **8**, 102148.
83 G. Lin, J. Tao, Y. Sun, Y. Cui, I. Manners and H. Qiu, *J. Am. Chem. Soc.*, 2024, **146**, 14734–14744.
84 D. Chakraborty, W. Ma, P. G. Vekilov and J. D. Rimer, *Chem. Mater.*, 2025, **37**, 4158–4168.
85 Y. Li, X. Shan, S. Li, J. Wang, Z. Li, Z. Wang, X. Li, W. Hong, M. Li and Y. Ma, *Angew. Chem., Int. Ed.*, 2023, **62**, e202311778.
86 H. Kim, J. Lee, S.-H. Hwang, N. Yun, S. Park and T.-L. Choi, *J. Am. Chem. Soc.*, 2024, **146**, 20750–20757.
87 Z. Wang, Q. Liang, M. Li, G. Sun, S. Li, T. Zhu, Y. Han, H. Xia, Z. Ren, B. Yu, J. Zhang, R. Ma, H. Thachoth Chandran, L. Cheng, L. Zhang, D. Li, S. Chen, X. Lu, C. Yan, R. Azmi, K. Liu, J. Tang and G. Li, *Adv. Mater.*, 2025, **37**, 2418011.
88 G. Lu, H. A, Y. Zhao, Y. Zhao, H. Xu, W. Shang, X. Chen, J. Sun, H. Zhang, J. Wu, B. Dai, B. Van der Bruggen, R. Dewil, A. K. An and S. Zheng, *Nat. Commun.*, 2025, **16**, 2284.
89 X. Wu, W. Yuan, Y. Wu, C. Wang, L. Xue, Y. Zhou, X. Zhang, S. Jiang, B. Zhao, Y. Chen, C. Yang, L. Ding, Y. Tang and X. Ding, *Adv. Energy Mater.*, 2024, **14**, 2304204.
90 Y. Shen, S. Zhang, Z. Qin, A. Beuque, L. Pinard, S. Asahina, N. Asano, R. Zhang, J. Zhao, Y. Fan, X. Liu, Z. Yan and S. Mintova, *ACS Catal.*, 2024, **14**, 3766–3777.
91 J. Tian, S.-H. Xie, U. Borucu, S. Lei, Y. Zhang and I. Manners, *Nat. Mater.*, 2023, **22**, 786–792.
92 Y. Lu, J. Tao, Z. Li, S. Wang, X. Cai and H. Qiu, *J. Am. Chem. Soc.*, 2026, **148**, 3158–3166.
93 H. Wang, X. Wang, M. A. Winnik and I. Manners, *J. Am. Chem. Soc.*, 2008, **130**, 12921–12930.
94 X.-S. Wang, H. Wang, N. Coombs, M. A. Winnik and I. Manners, *J. Am. Chem. Soc.*, 2005, **127**, 8924–8925.
95 H. Qiu, V. A. Du, M. A. Winnik and I. Manners, *J. Am. Chem. Soc.*, 2013, **135**, 17739–17742.
96 J. Tao, B. Fang, Z. Fang, G. Lin, Z. Ji, C. Gao, R. Gao and H. Qiu, *Angew. Chem., Int. Ed.*, 2025, **64**, e202512348.
97 S. Wang, W. Xie, P. Wu, G. Lin, Y. Cui, J. Tao, G. Zeng, Y. Deng and H. Qiu, *Nat. Commun.*, 2022, **13**, 6673.